Molybdophosphonate Clusters as Building Blocks in the Oxomolybdate-Organodiphosphonate/Cobalt(II)–Organoimine System: Structural Influences of Secondary Metal Coordination Preferen...

7 AUTHORS, INCLUDING:

Damian G Allis

Syracuse University

60 PUBLICATIONS   **1,147** CITATIONS

SEE PROFILE

Andrey Prosvirin

Texas A&M University

97 PUBLICATIONS   **2,792** CITATIONS

SEE PROFILE

Kim R Dunbar

Texas A&M University

443 PUBLICATIONS   **13,384** CITATIONS

SEE PROFILE

Jon Zubieta

Syracuse University

790 PUBLICATIONS   **24,896** CITATIONS

SEE PROFILE

Inorganic Chemistry

Molybdophosphonate Clusters as Building Blocks in the Oxomolybdate-Organodiphosphonate/Cobalt(II)–Organoimine System: Structural Influences of Secondary Metal Coordination Preferences and Diphosphonate Tether Lengths

N. Gabriel Armatas,[†] Damian G. Allis,[†] Andrew Prosvirin,[‡] Gabriel Carnutu,[§] Charles J. O'Connor,[§] Kim Dunbar,[‡] and Jon Zubieta*,[†]

Department of Chemistry, Syracuse University, Syracuse, New York 13244, Department of Chemistry, Texas A&M University, College Station, Texas 77843, and Department of Chemistry, University of New Orleans, New Orleans, Louisiana 70148

Hydrothermal conditions have been used in the preparation of a series of organic–inorganic hybrid materials of the cobalt–molybdophosphonate family. The reactions of MoO_3, cobalt(II) acetate or cobalt(II) acetylacetonate, tetra-2-pyridylpyrazine (tpyprz), and organodiphosphonic acids $H_2O_3P(CH_2)_nPO_3H_2$ ($n = 1$–5 and 9) of varying tether lengths yielded compounds of the general type $\{Co_2(tpyprz)(H_2O)_m\}^{4+}/Mo_xO_y\{O_3P(CH_2)_nPO_3\}_z$. The recurring theme of the structural chemistry is the incorporation of $\{Mo_5O_{15}(O_3PR)_2\}^{4-}$ clusters as molecular building blocks observed in the structures of nine phases (compounds **2**–**9** and **11**). The structural consequences of variations in reaction conditions are most apparent in the series with propylene diphosphonate, where four unique structures **4**–**7** are observed, including two distinct three-dimensional architectures for compounds **5** and **6** whose formulations differ only in the number of water molecules of crystallization. With pentyldiphosphonate, a second phase **10** is obtained which exhibits a unique cluster building block, the hexamolybdate $[Mo_6O_{18}\{O_3P(CH_2)_5PO_3\}]^{4-}$. In the case of methylenediphosphonic acid, a third structural motif, the trinuclear $\{(Mo_3O_8)(O_3PCH_2PO_3)\}^{2-}$ subunit, is observed in compound **1**. The structural chemistry of compounds **1**–**11** of this study is quite distinct from that of the $\{Ni_2(tpyprz)(H_2O)_m\}^{4+}/Mo_xO_y\{O_3P(CH_2)_nPO_3\}_z$ family, as well as that of the copper-based family. The structural diversity of this general class of materials reflects the coordination preferences of the M(II) sites, the extent of aqua ligation to the M(II) sites, the participation of both phosphate oxygen atoms and molybdate oxo-groups in linking to the M(II) sites, and the variability in the number of attachment sites at the molybdophosphonate clusters. Since the charge densities at the peripheral oxygen atoms of the clusters are quite uniform, the attachment of $\{M_2(tpyprz)\}^{4+}$ subunits to the molybdophosphonates appears to be largely determined by steric, coulombic, and packing factors, as shown by extensive density functional theory calculations.

Introduction

Inorganic oxides are ubiquitous materials, distinguished by their unusual compositional range and structural versatility,[1,2] characteristics reflected in their extensive physical properties and applications ranging from heavy construction to molecular electronics.[3–11] The fundamental and practical

* To whom correspondence should be addressed. E-mail: jazubiet@syr.edu.
† Syracuse University.
‡ Texas A&M University.
§ University of New Orleans.

(1) Greenwood, N. N.; Earnshaw, A. *Chemistry of the Elements*; Pergamon Press: New York, 1984.
(2) Wells, A. F. *Structural Inorganic Chemistry*, 4th ed.; Oxford University Press: Oxford, U.K., 1978.
(3) McCarroll, W. H. In *Encyclopedia of Inorganic Chemistry*; King, R. B., Ed.; Wiley: New York, 1994; Vol. 6, pp 2903−2946.
(4) Bruce, D. W., O'Hare, D., Eds. *Inorganic Materials;* Wiley: Chichester, U.K., 1992.
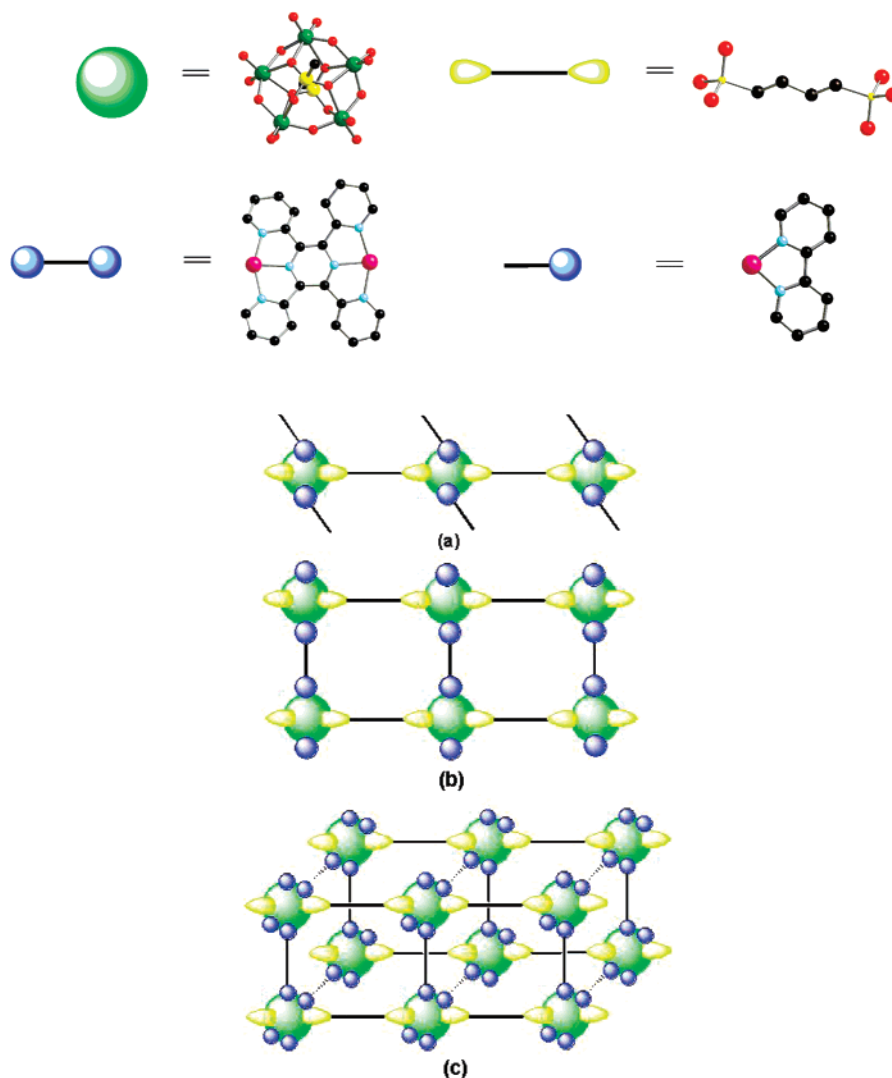(5) Cheetham, A. K. *Science* **1964**, *264*, 794.
(6) Cockayne, B., James, D. W., Eds. *Modern Oxide Materials*; Academic Press; New York, 1972.
(7) Büchner, W.; Schliebs, R.; Winter, G.; Büchel, K. H. *Industrial Inorganic Chemistry*; VCH: New York, 1989.
(8) Okuhara, T.; Misono, M. *Encyclopedia of Inorganic Chemistry*; Wiley: New York, 1994; Vol. 6, p 2889.
(9) Clearfield, A. *Chem. Rev.* **1988**, *88*, 125.

Scheme 1

importance of these materials drives efforts toward the predictable modification of oxide microstructures and the design of novel materials.

One approach to synthesis of new oxide materials exploits the "bottom-up" strategy of linking molecular oxide building blocks through appropriate organic molecules or secondary

metal cations.[12−20] The vast family of molecular oxides commonly referred to as polyoxometalates provides robust clusters of different sizes,[21−26] topologies, and oxidation states for the construction of solids with more or less predictable connectivity in the crystalline state. Appropriate ligand bridges should thus provide linkages sufficiently strong to connect the clusters into kinetically stable, crystalline architectures.

We have recently demonstrated this approach using a three-component system consisting of a molybdenum oxide cluster, a tethering organic component, and a secondary metal coordination complex cation.[27−34] As illustrated in Scheme

(10) Newsam, J. M. *Solid State Compounds*; Clarendon Press: Oxford, U.K., 1992; p 234.
(11) Landau, M. V. Transition Metal Oxides. *Handbook of Porous Solids*; Wiley-VCH: Weinheim, Germany, 2002; Vol. 3, pp 1677−1765.
(12) Hagrman, P. J.; Hagrman, D.; Zubieta, J. *Angew. Chem., Int. Ed.* **1999**, *38*, 2638.
(13) DeBord, J. R. D.; Haushalter, R. C.; Meyer, C. M.; Rose, D. J.; Zapf, P. J.; Zubieta, J. *Inorg. Chim. Acta* **1997**, *256*, 165.
(14) Khan, M. I.; Yohannes, E.; Doedens, R. J. *Angew. Chem., Int. Ed.* **1999**, *38*, 1292.
(15) Khan, M. I.; Yohannes, E.; Doedens, R. J. *Inorg. Chem.* **2003**, *42*, 3125, and references therein.
(16) Chen, J.; Lu, S.; Yu, R.; Chen, Z.; Huang, Z.; Lu, C. *Chem. Commun. (Cambridge)* **2002**, 2640.
(17) Linnard, L.; Dolbecq, A.; Mialene, P.; Marrot, J.; Secheresse, F. *Inorg. Chem. Acta* **2004**, *357*, 845.
(18) Farrette, S.; Hasenknopf, B.; Vaissermann, J.; Gouzerk, P.; Roux, C. *Chem. Commun. (Cambridge)* **2003**, 2664.
(19) Lin, B. Z.; Chen, Y.-M.; Liu, P.-D. *Dalton Trans.* **2003**, 2474.
(20) Finn, R. C.; Sims, J.; O'Connor, C. J.; Zubieta, J. *J. Chem. Soc., Dalton Trans.* **2002**, 159, and references therein.

(21) Special thematic issue on polyoxometalates: Hill, C. L., Ed. *Chem. Rev.* **1998**, *98*, 1−387.
(22) *Polyoxometalate Chemistry: From Topology Via Self-Assembly to Applications*; Pope, M. T., Muller, A., Eds.; Kluwer Academic: Dordrecht, The Netherlands, 2001.
(23) Pope, M. T. *Heteropoly and Isopoly Oxometalates*; Springer: Berlin, 1983.
(24) *Polyoxometalates: From Platonic Solids to Anti-Retroviral Activity*; Pope, M. T., Muller, A., Eds.; Kluwer Academic: Dordrecht, The Netherlands, 1994.
(25) Jolivet, J.-P. *Metal Oxide Chemistry and Synthesis: From Solution to Solid State*; Wiley: New York, 2000.
(26) Katnoulis, D. E. *Chem. Rev.* **1998**, *98*, 359.

1, the "venerable" polyoxomolybdates[35−37] $[Mo_5O_{15}(O_3PR)_2]^{4-}$ and $[Mo_6O_{18}(O_3AsR)_2]^{4-}$ are readily tethered through organic chains of diphosphonate ligands $\{O_3E\text{-tether-}EO_3\}^{4-}$ (E = P, As) into one-dimensional structures.[38] However, charge-compensation and space-filling requirements were most effectively satisfied by a secondary metal coordination complex, such as $\{Cu(bpy)\}^{2+}$ or $\{Cu(phen)\}^{2+}$. Consequently, it was realized that structural expansion into two and three dimensions could be effected by the use of appropriate secondary metals and binucleating ligands. In these structures, the molybdate cluster acts as a node and structural elaboration depends on the number of surface accessible binding sites, in a manner reminiscent of metal organic frameworks (MOFs).[39−46]

In the course of these investigations, a number of structural determinants were identified: (i) the cluster size which correlates with the number of linkage sites on the oxide surface, (ii) the identity of the pnictide, whether phosphorus or arsenic, (iii) the tether length and/or functionality of the diphosphonate bridge, and (iv) the coordination preferences of the secondary metal. This latter point was effectively illustrated in comparing the structural chemistries of the Cu-(II) and Ni(II) series of Mo_xO_y/diphosphonate/M(II)−organonitrogen families of bimetallic oxides. While Cu(II) displays Jahn−Teller distorted geometries (square planar and

4 + 1 and 4 + 2 axially distorted polyhedra), Ni(II) exhibits more regular octahedral coordination. The consequences of these contrasting coordination preferences are reflected in the structures of materials constructed with tetra-2-pyridinylpyrazine as the ligand to the secondary metal. While Cu-(II) binds exclusively to a single terminus of the tetrapyridylpyrazine (tpyprz) ligand to form $\{Cu_2(tpyprz)\}^{4+}$ moieties, adopting $\{CuN_3O\}$, $\{CuN_3O_2\}$, or $\{CuN_3O_3\}$ coordination modes upon linking to the oxide substructure, through one, two, or three attachment points, respectively, Ni(II) may adopt more regular octahedral geometry by coordinating to two tpyprz ligands to give $\{NiN_6\}$ coordination geometry. The balance between this proclivity toward regular six coordination and the oxophilicity of Ni(II) resulted in varying degrees of catenation $\{Ni(tpyprz)\}_n^{2n+}$, a feature which dramatically expanded the structural chemistry of the materials of the Mo_xO_y/diphosphonate/M(II)−tpyprz family.

These results encouraged us to expand our studies to the Co(II) analogues. The naive expectation was that the structural chemistry would be analogous to that of Ni(II). In fact, while some analogies do exist, the results were largely unanticipated. The syntheses, structures, and magnetic properties of members of Mo_xO_y/diphosphonate/Co(II)−tpyprz are reported: $[Co(H_2tpyprz)_2][(Mo_3O_8)_3(O_3PCH_2PO_3)_3]\cdot7H_2O\cdot C_5H_5N$ (**1**·7H₂O·py), $[\{Co_4(tpyprz)_3\}(Mo_5O_{15})_2(O_3PCH_2CH_2PO_3)_2]\cdot18H_2O$ (**2**·18H₂O), $[\{Co(H_2tpyprz)\}Mo_5O_{15}\{O_3PCH_2CH_2PO_3\}]$ (**3**), $[\{Co_2(tpyprz)_2\}Mo_5O_{15}\{O_3P(CH_2)_3PO_3\}]\cdot5H_2O$ (**4**·5H₂O), $[\{Co_2(tpyprz)(H_2O)_3\}Mo_5O_{15}\{O_3P(CH_2)_3PO_3\}]\cdot7H_2O$ (**5**·7H₂O), $[\{Co_2(tpyprz)(H_2O)_3\}Mo_5O_{15}\{O_3P(CH_2)_3PO_3\}]\cdot H_2O$ (**6**·H₂O), $[H_3O]_2[\{Co_3(tpyprz)_2(H_2O)_3\}(Mo_5O_{15})_2\{O_3P(CH_2)_3PO_3\}_2]\cdot21.4H_2O$ (**7**·21.4H₂O), $[\{Co_2(tpyprz)(H_2O)_2\}Mo_5O_{15}\{O_3P(CH_2)_4PO_3\}]\cdot2H_2O$ (**8**·2H₂O), $[\{Co_2(tpyprz)(H_2O)_3\}Mo_5O_{15}\{O_3P(CH_2)_5PO_3\}]\cdot2.5H_2O$ (**9**·2.5H₂O), $[\{Co_2(tpyprz)(H_2O)_2\}Mo_6O_{18}\{O_3P(CH_2)_5PO_3\}]\cdot2H_2O$ (**10**·2H₂O), and $[\{Co_2(tpyprz)(H_2O)_3\}Mo_5O_{15}\{O_3P(CH_2)_9PO_3\}]\cdot2.5H_2O$ (**11**·2.5H₂O). The structures of $[Co(bpy)_3][Mo_5O_{14}(OH)\{HO_3P(CH_2)_2PO_3\}]\cdot H_2O$ (**12**·H₂O), $[Co(terpy)_2][Mo_5O_{14}(OH)\{HO_3P(CH_2)_3PO_3\}]\cdot H_2O$ (**13**·H₂O), and $[\{Co_2(phen)_3(H_2O)\}Mo_5O_{15}\{O_3P(CH_2)_3PO_3\}]$ (**14**), where the binucleating tpyprz ligand has been replaced by 2,2′-bipyridine (bpy), o-phenanthroline (phen), or terpyridine (terpy), are also described.

Experimental Procedures

Materials and General Procedures. Chemicals were used as obtained without further purification with the exception of the diphosphonic acids (n = 3−5), which were synthesized by slight modification of the reported methods.[47−49] Tetra-2-pyridinylpyrazine was purchased from Aldrich; cobalt(II) acetate tetrahydrate, cobalt-(II) 2,4-pentanedionate, acetic acid, molybdenum(VI) oxide (99.5%), methylenediphosphonic acid, and 1,2-ethylenediphosphonic acid were purchased from Alfa Aesar. All syntheses were carried out in 23 mL of poly(tetrafluoroethylene) lined stainless steel containers under autogenous pressure. The reactants were stirred briefly, and

(27) Finn, R. C.; Zubieta, J. *Inorg. Chem.* **2001**, *40*, 2466.
(28) Burkholder, E.; Zubieta, J. *Chem. Commun. (Cambridge)* **2001**, 2056.
(29) Finn, R. C.; Burkholder, E.; Zubieta, J. *Chem. Commun. (Cambridge)* **2001**, 1852.
(30) Finn, R. C.; Rarig, R. S.; Zubieta, J. *Inorg. Chem.* **2002**, *41*, 2109.
(31) Burkholder, E.; Wright, S.; Golub, V.; O'Connor, C. J.; Zubieta, J. *Inorg. Chem.* **2003**, *42*, 7460.
(32) Burkholder, E.; Golub, V.; O'Connor, C. J.; Zubieta, J. *Inorg. Chem.* **2003**, *42*, 6729.
(33) Burkholder, E.; Golub, V.; O'Connor, C. J.; Zubieta, J. *Chem. Commun. (Cambridge)* **2003**, 2128.
(34) Burkholder, E.; Golub, V.; O'Connor, C. J.; Zubieta, J. *Inorg. Chem.* **2004**, *43*, 7014.
(35) Kwak, W.; Pope, M. T.; Scully, T. F. *J. Am. Chem. Soc.* **1975**, *97*, 5735.
(36) Hedman, B. *Acta Crystallogr.* **1980**, *B36*, 2241.
(37) Kwak, W.; Rajkovic, L. M.; Stalick, J. K.; Pope, M. T.; Quicksall, C. O. *Inorg. Chem.* **1976**, *15*, 2778.
(38) The chemistry of the metal organophosphonates has witnessed remarkable growth in the past decade. A number of useful reviews is available: (a) Vioux, A.; LeBideau, J.; Mutin, P. H.; Leclercq, D. *Top. Curr. Chem.* **2004**, *232*, 145. (b) Clearfield, A. *Curr. Opin. Solid State Mater. Sci.* **2002**, *6*, 495. (c) Clearfield, A. *Prog. Inorg. Chem.* **1998**, *47*, 371. (d) Alberti, G. In *Comprehensive Supramolecular Chemistry*; Atwood, J. L., Davis, J. E. D., Vogel, F., Eds.; Pergamon Press: New York, 1996; Vol. 9 (Alberti, G., Bein, T., Eds.), p 152. (e) Clearfield, A. In *Comprehensive Supramolecular Chemistry*; Atwood, J. L., Davis, J. E. D., Vogel, F., Eds.; Pergamon Press: New York, 1996; Vol. 9 (Alberti, G., Bein, T., Eds.), p 107. (f) Clearfield, A. *Chem. Mater.* **1998**, *10*, 2801. (g) Vermeulen, L. A. *Prog. Inorg. Chem.* **1997**, *44*, 143.
(39) Sudik, A. C.; Millward, A. R.; Ockwig, N. W.; Coté, A. P.; Kim, J.; Yaghi, O. M. *J. Am. Chem. Soc.* **2005**, *127*, 7110.
(40) Forster, P. M.; Cheetham, A. K. *Top. Catal.* **2003**, *24*, 79.
(41) Janiak, C. *Dalton Trans.* **2003**, 2781.
(42) Batten, S. R.; Robson, R. *Angew. Chem., Int. Ed.* **1998**, *37*, 1461, and references therein.
(43) Sommerdijk, J. M. *Angew. Chem., Int. Ed.* **2003**, *42*, 3572, and references therein.
(44) Papaefstathiou, G. S.; MacGillivray, L. R. *Coord. Chem. Rev.* **2003**, *246*, 169.
(45) Rosi, N. L.; Eddaoudi, M.; Kim, J.; O'Keeffe, M.; Yaghi, O. M. *Cryst. Eng. Commun.* **2002**, *4*, 401.
(46) Yaghi, O. M.; O'Keeffe, M.; Ockwig, N. W.; Chase, H. K.; Eddaoudi, M.; Kim, J. *Nature* **2003**, *423*, 705.

(47) McKenna, C. E.; Higa, M. T.; Cheung, N. H.; McKenna, M. C. *Tetrahedron Lett.* **1977**, 155.
(48) Wang, Z.; Heising, J. M.; Clearfield, A. *J. Am. Chem. Soc.* **2003**, *125*, 10375.
(49) Arnold, D. I.; Ouyang, X.; Clearfield, A. *Chem. Mater.* **2002**, *14*, 2020.

the initial pH was measured before heating. Water was distilled above 3.0 MΩ in-housing using a Barnstead model 525 Biopure distilled water center. The initial and final pH of each reaction were measured using color pHast sticks. Infrared spectra were obtained on a Perkin-Elmer 1600 series FTIR spectrometer. Sample purities were confirmed by powder X-ray diffraction (XRD). In several cases, some amorphous materials coprecipitated with the crystalline products. The crystals were separated from the powders either by manual method or by flotation in appropriate solvents.

Synthesis of [Co(H₂tpyprz)₂][(Mo₃O₈)₃(O₃PCH₂PO₃)₃]·7H₂O·C₅H₅N (1·7H₂O·py). A mixture of MoO_3 (0.195 g, 1.355 mmol), $Co(O_2CCH_3)_2·4H_2O$ (0.055 g, 0.221 mmol), tpypyz (0.086 g, 0.221 mmol), $H_2PO_3CH_2PO_3H_2$ (0.056 g, 0.318 mmol), H_2O (10 g, 555 mmol), and concentrated CH_3COOH (0.125 g) in the ratio of 6.1:1.0:1.0:1.44:2511 was stirred briefly before being heated to 180 °C for 72 h. Red platelike crystals of **1**·7H₂O·py were isolated in 26% yield (initial pH, 2; final pH, 2.5). IR (KBr pellet, cm⁻¹): 3072 (m, br), 2999 (s), 1593 (w), 1479 (w), 1401 (m), 1168 (m), 1090 (m), 1062 (s), 952 (s), 907 (s), 739 (s), 658 (m).

Synthesis of [{Co₄(tpyprz)₃}Mo₅O₁₅{O₃P(CH₂)₂PO₃}₂]·18H₂O (2·18H₂O). A solution of MoO_3 (0.196 g, 1.362 mmol), $Co(O_2CCH_3)_2·4H_2O$ (0.055 g, 0.221 mmol), tpyprz (0.086 g, 0.221 mmol), $H_2PO_3(CH_2)_2PO_3H_2$ (0.086 g, 0.453 mmol), H_2O (10 g, 555 mmol), and concentrated CH_3COOH (0.125 g) in the mole ratio of 6.15:1.00:1.00:2.04:2511 was stirred briefly before being heated to 170 °C for 72 h (initial pH, 2; final pH, 2.5). Red crystals of **2**·18H₂O, suitable for X-ray studies, were isolated in 32% yield. IR (KBr pellet, cm⁻¹): 2917 (s), 1634 (m), 1593 (m), 1540 (w), 1454 (w), 1417 (w), 1385 (w), 1197 (m), 1115 (s), 1046 (s), 927 (s), 902 (s), 727 (s), 690 (s), 620 (m), 551 (m).

Synthesis of [{Co(H₂tpyprz)}Mo₅O₁₅{O₃P(CH₂)₂PO₃}] (3). A mixture of MoO_3 (0.196 g, 1.362 mmol), $Co(O_2CCH_3)_2·4H_2O$ (0.055 g, 0.221 mmol), tpypyz (0.086 g, 0.221 mmol), $H_2PO_3(CH_2)_2PO_3H_2$ (0.086 g, 0.453 mmol), H_2O (10 g, 555 mmol), and concentrated CH_3COOH (0.125 g) in the mole ratio of 6.15:1.00:1.00:2.04:2511 was stirred briefly before being heated to 180 °C for 72 h. Red crystals of **3** were isolated in 42% yield (initial pH, 2; final pH, 2.5). IR (KBr pellet, cm⁻¹): 3080 (s, br), 2921 (w), 1614 (w), 1409 (w), 1205 (w), 1119 (s), 1082 (m), 1058 (m), 935 (s, br), 776 (s), 682 (s, br).

Synthesis of [{Co₂(tpyprz)₂}Mo₅O₁₅{O₃P(CH₂)₃PO₃}]·5H₂O (4·5H₂O). The reaction of MoO_3 (0.198 g, 1.375 mmol), $Co(O_2CCH_3)_2·4H_2O$ (0.054 g, 0.217 mmol), tpypyz (0.158 g, 0.221 mmol), $H_2PO_3(CH_2)_3PO_3H_2$ (0.090 g, 0.441 mmol), H_2O (10 g, 555 mmol), and concentrated CH_3COOH (0.125 g) in the mole ratio of 3.38:0.53:1.00:1.08:2511 at 180 °C for 96 h gave red crystals of **4**·5H₂O in 45% yield (initial pH, 2.0; final pH, 3.0). IR (KBr pellet, cm⁻¹): 3072 (s, br), 1589 (m), 1475 (w), 1405 (s), 1254 (w), 1201 (w), 1152 (w), 1099 (w), 1058 (m), 931 (s), 903 (s), 800 (s), 703 (s, br), 575 (m).

Synthesis of [{Co₂(tpyprz)(H₂O)₃}Mo₅O₁₅{O₃P(CH₂)₃PO₃}]·7H₂O (5·7H₂O). A solution of MoO_3 (0.196 g, 1.362 mmol), $Co(O_2CCH_3)_2·4H_2O$ (0.056 g, 0.225 mmol), tpypyz (0.086 g, 0.221 mmol), $H_2PO_3(CH_2)_3PO_3H_2$ (0.090 g, 0.441 mmol), H_2O (10 g, 555 mmol), and concentrated CH_3COOH (0.125 g) in the mole ratio of 6.15:1.02:1.00:1.99:2511 at 180 °C for 96 h yielded red crystals of **5**·7H₂O, suitable for X-ray diffraction in 52% yield (initial pH, 2.0; final pH, 3.0). IR (KBr pellet, cm⁻¹): 2921 (s, br), 2864 (s), 1597 (m), 1475 (w), 1409 (m), 1303 (w), 1254 (w), 1197 (w), 1099 (m), 1033 (m), 976 (m), 927 (s), 890 (s), 866 (s), 784 (w), 665 (s), 565 (m).

Synthesis of [{Co₂(tpyprz)(H₂O)₃}Mo₅O₁₅{O₃P(CH₂)₃PO₃}]·H₂O (6·H₂O). A solution of MoO_3 (0.158 g, 1.098 mmol), Co-(O₂CCH₃)₂·4H₂O (0.058 g, 0.226 mmol), tpypyz (0.085 g, 0.219 mmol), $H_2PO_3(CH_2)_3PO_3H_2$ (0.090 g, 0.441 mmol), H_2O (10 g, 555 mmol), and concentrated CH_3COOH (0.125 g) in the mole ratio of 5.02:1.03:1.00:2.02:2511 was stirred briefly before being heated to 200 °C for 96 h. Red crystals of **6**·H₂O suitable for X-ray diffraction were isolated in 32% yield (initial pH, 2.0; final pH, 2.5). IR (KBr pellet, cm⁻¹): 2921 (s), 1597 (m), 1474 (w), 1400 (m), 1200 (w), 1139 (w), 1098 (m), 1029 (w), 928 (s), 783 (m), 681 (s, br), 575 (w).

Synthesis of [H₃O]₂[{Co₃(tpyprz)₂(H₂O)₃}{Mo₅O₁₅(O₃P(CH₂)₃PO₃)}₂]·21.4H₂O (7·21.4H₂O). A mixture of MoO_3 (0.157 g, 1.091 mmol), Co(acac)₂ (0.058 g, 0.226 mmol), tpypyz (0.084 g, 0.216 mmol), $H_2PO_3(CH_2)_3PO_3H_2$ (0.090 g, 0.441 mmol), H_2O (10 g, 555 mmol), and concentrated CH_3COOH (0.125 g) in the mole ratio of 5.04:1.04:1.00:2.04:2511 was stirred briefly before being heated to 200 °C for 72 h. Red crystals of **7**·21.4H₂O were isolated in 18% yield (initial pH, 2.0; final pH, 2.5). IR (KBr pellet, cm⁻¹): 3068 (s, br), 2913 (s), 1589 (m), 1475 (w), 1405 (m), 1306 (w), 1201 (w), 1107 (w), 1058 (w), 927 (s), 907 (s), 698 (s), 575 (w). Valance sum calculations confirmed the assignment of the cobalt sites as Co(II), and the phosphonate oxygen atoms are not protonated. Consequently, charge balance requirements necessitate that there be hydronium cations present. While oxygen atom positions were identified from the difference maps, hydrogen atoms were not found, leaving ambiguous the identities of the hydronium cations.

Synthesis of [{Co₂(tpyprz)(H₂O)₂}Mo₅O₁₅{O₃P(CH₂)₄PO₃}]·2H₂O (8·2H₂O). The reaction of MoO_3 (0.158 g, 1.098 mmol), $Co(O_2CCH_3)_2·4H_2O$ (0.054 g, 0.217 mmol), tpypyz (0.087 g, 0.224 mmol), $H_2PO_3(CH_2)_4PO_3H_2$ (0.097 g, 0.445 mmol), H_2O (10 g, 555 mmol), and concentrated CH_3COOH (0.125 g) in the mole ratio of 4.90:1.01:1.00:2.01:2511 at 200 °C for 96 h provided orange blocks of **8**·2H₂O in 35% yield (initial pH, 2.0; final pH, 3.0). IR (KBr pellet, cm⁻¹): 2942 (s), 1618 (w), 1397 (w), 1185 (w), 1103 (m), 1074 (w), 1058 (w), 939 (s), 780 (w), 747 (w), 572 (w).

Synthesis of [{Co₂(tpyprz)(H₂O)₃}Mo₅O₁₅{O₃P(CH₂)₅PO₃}]·2.5H₂O (9·2.5H₂O). The reaction of MoO_3 (0.159 g, 1.105 mmol), $Co(O_2CCH_3)_2·4H_2O$ (0.110 g, 0.442 mmol), tpyprz (0.086 g, 0.221 mol), $H_2PO_3(CH_2)_5PO_3H_2$ (0.051 g, 0.212 mmol), H_2O (10 g, 555 mmol), and concentrated CH_3COOH (0.125 g) in the mole ratio of 5.0:2.0:1.0:0.96:2511 at 180 °C for 72 h provided orange platelike crystals of **9**·2.5H₂O suitable for X-ray diffraction in 34% yield (initial pH, 2.0; final pH, 2.5). IR (KBr pellet, cm⁻¹): 2964 (s, br), 2921 (s), 1597 (m), 1458 (w), 1397 (m), 1313 (w), 1254 (w), 1225 (w), 1152 (w), 1099 (m), 1108 (m), 1011 (m), 931 (s), 892 (s), 866 (s), 784 (s), 678 (s, br), 559 (m).

Synthesis of [{Co₂(tpyprz)(H₂O)₂}Mo₆O₁₈{O₃P(CH₂)₅PO₃}]·2H₂O (10·2H₂O). A solution of MoO_3 (0.196 g, 1.362 mmol), Co-(O₂CCH₃)₂·4H₂O (0.56 g, 0.225 mmol), tpypyz (0.085 g, 0.221 mmol), $H_2PO_3(CH_2)_5PO_3H_2$ (0.102 g, 0.439 mmol), H_2O (10 g, 555 mmol), and concentrated CH_3COOH (0.125 g) in the mole ratio of 6.16:1.02:1:1.99:2511 was stirred briefly before being heated to 180 °C for 72 h (initial pH, 2.5; final pH, 2.0). Red octahedral shaped crystals of **10**·2H₂O suitable for X-ray studies, were isolated in 13% yield. IR (KBr pellet, cm⁻¹): 3064 (s, br), 2921 (s), 1597 (m), 1458 (w), 1397 (m), 1303 (w), 1254 (w), 1205 (w), 1152 (w), 1099 (m), 1058 (m), 1001 (m), 931 (s), 886 (s), 866 (s), 784 (s), 678 (s, br), 559 (m).

Synthesis of [{Co₂(tpyprz)(H₂O)₃}Mo₅O₁₅{O₃P(CH₂)₉PO₃}]·2.5H₂O (11·2.5H₂O). The reaction of MoO_3 (0.157 g, 1.091 mmol), $Co(O_2CCH_3)_2·4H_2O$ (0.054 g, 0.217 mmol), tpypyz (0.085 g, 0.219 mmol), $H_2PO_3(CH_2)_9PO_3H_2$ (0.127 g, 0.441 mmol), H_2O (10 g, 555 mmol), and concentrated CH_3COOH (0.125 g) in the mole ratio of

Table 1. Summary of Crystallographic Data

	1	**2**	**3**	**4**	**5**	**6**	**7**
empirical formula	$C_{56}H_{61}CoMo_9$- $N_{13}O_{49}P_6$	$C_{38}H_{46}Co_2Mo_5$- $N_9O_{31}P_2$	$C_{26}H_{24}CoMo_5$- $N_6O_{22}P_2$	$C_{51}H_{48}Co_2Mo_5$- $N_{12}O_{26}P_2$	$C_{27}H_{42}Co_2Mo_5$- $N_6O_{31}P_2$	$C_{27}H_{30}Co_2Mo_5$- $N_6O_{25}P_2$	$C_{54}H_{96.8}Co_3Mo_{10}$- $N_{12}O_{68.4}P_4$
fw	2808.39	1784.34	1373.08	1904.51	1606.17	1498.07	3268.70
cryst syst	monoclinic	orthorhombic	orthorhombic	monoclinic	monoclinic	triclinic	monoclinic
space group	$P2_1/c$	Pbca	$Pna2_1$	$P2_1/n$	$P2_1/n$	$P\bar{1}$	$P2_1/n$
a, Å	17.927(1)	24.222(1)	15.3980(9)	16.421(2)	8.9070(7)	8.715(1)	18.2174(6)
b, Å	13.7114(9)	15.4803(7)	11.4633(7)	16.514(2)	18.932(1)	10.811(1)	20.2987(7)
c, Å	35.321(2)	30.616(1)	21.699(1)	25.093(2)	28.644(2)	22.274(3)	28.4749(9)
α, deg	90.0	90.0	90.0	90.0	90.0	88.800(2)	90.0
β, deg	102.26(2)	90.	90.	108.807(2)	98.641(2)	86.867(2)	98.947(1)
γ, deg	90.0	90.0	90.0	90.0	90.0	80.740(2)	90.0
V, Å	8483.8(10)	11480.1(9)	3830.2(4)	6441.5(10)	4775.3(6)	2068.1(4)	10401.6(6)
Z	4	8	4	4	4	2	4
D_{calc}, g cm^{-3}	2.199	2.065	2.381	1.964	2.234	2.406	2.087
μ, mm^{-1}	16.97	17.76	21.91	15.81	21.19	24.27	18.00
T, K	90(2)	90(2)	90(2)	90(2)	90(2)	90(2)	90(2)
λ, Å	0.710 73	0.710 73	0.710 73	0.710 73	0.710 73	0.710 73	0.710 73
largest diff peak and hole, e A^{-3}	1.093, −1.092	1.333, −0.945	0.771, −0.501	0.974, −0.499	1.342, −1.085	1.544, −1.308	1.349, −1.404
R_1 ^{a} (all data)	0.0742	0.0651	0.0268	0.0457	0.0461	0.0644	0.0683
R_{w2} ^{a} (all data)	0.1462	0.1365	0.0576	0.0872	0.0906	0.1446	0.1169
flack			0.0(03)				

	8	**9**	**10**	**11**	**12**	**13**	**14**
empirical formula	$C_{28}H_{32}Co_2Mo_5$- $N_6O_{25}P_2$	$C_{58}H_{72}Co_4Mo_{10}$- $N_{12}O_{52}P_4$	$C_{29}H_{34}Co_2Mo_6$- $N_6O_{28}P_2$	$C_{33}H_{45}Co_2Mo_5$- $N_6O_{26.5}P_2$	$C_{33}H_{32}CoMo_5$- $N_6O_{22}P_2$	$C_{33}H_{30}CoMo_5$- $N_6O_{22}P_2$	$C_{39}H_{42}Co_2Mo_5$- $N_6O_{27}P_2$
fw	1512.10	3088.28	1670.06	1609.25	1465.22	1463.20	1686.29
cryst syst	triclinic	monoclinic	orthorhombic	monoclinic	monoclinic	monoclinic	monoclinic
space group	$P\bar{1}$	$P2_1/c$	$P2_12_12_1$	$P2_1/c$	$P2_1/c$	$P2_1/c$	$C2/c$
a, Å	12.483(2)	32.571(3)	11.3379(6)	13.0322(5)	8.8546(7)	8.8341(7)	30.734(4)
b, Å	12.931(2)	13.002(1)	13.4184(7)	13.6995(6)	31.263(3)	30.889(2)	16.205(2)
c, Å	13.535(2)	21.235(2)	29.880(2)	27.258(1)	15.927(1)	15.435(1)	26.204(3)
α, deg	96.996(3)	90.0	90.0	90.0	90.0	90.0	90.0
β, deg	98.973(3)	91.283(2)	90.	96.820(1)	98.151(2)	90.180(2)	121.562(2)
γ, deg	93.022(3)	90.0	90.0	90.0	90.0	90.0	90.0
V, Å	2136.2(7)	8991(1)	4545.8(4)	4832.1(3)	4364.5(6)	4211.9(9)	11120(3)
Z	2	4	4	4	4	4	8
D_{calc}, g cm^{-3}	2.351	2.282	2.440	2.212	2.230	2.307	2.015
μ, mm^{-1}	23.51	22.39	24.83	20.88	19.30	20.00	18.21
T, K	90(2)	90(2)	90(2)	90(2)	90(2)	90(2)	90(2)
λ, Å	0.71073	0.71073	0.71073	0.71073	0.71073	0.71073	0.71073
largest diff peak and hole, e A^{-3}	1.418, −1.361	1.075, −1.527	1.563, −0.942	1.057, −0.991	0.903, −0.744	0.856, −0.910	0.824, −0.623
R_1 ^{a} (all data)	0.0648	0.0861	0.0780	0.0667	0.0491	0.0324	0.0533
R_{w2} ^{a} (all data)	0.1106	0.1641	0.1264	0.1127	0.0916	0.0742	0.0863
flack			0.0(07)				

^{a} $R_1 = \sum|F_o| - |F_c|/\sum|F_o|$. $R_{w2} = \{\sum[w(F_o^2 - F_c^2)^2]/\sum[w(F_o^2)^2]\}^{1/2}$.

4.98:0.99:1:2.01:2534 at 200 °C for 96 h gave dark red blocks of **11**·2.5H$_2$O in 25% yield (initial pH, 1.5; final pH, 2.5). IR (KBr pellet, cm^{-1}): 2921 (s), 2848 (s), 1593 (m), 1475 (m), 1450 (w), 1409 (m), 1303 (w), 1254 (w), 1205 (w), 1156 (w), 1103 (s), 1066 (m), 1037 (m), 1001 (m), 935 (s), 890 (s), 788 (m), 686 (s, br), 563 (m).

Synthesis of [Co(bpy)$_3$][Mo$_5$O$_{14}$(OH){HO$_3$P(CH$_2$)$_3$PO$_3$}]·H$_2$O (12·H$_2$O). A solution of MoO$_3$ (0.157 g, 1.091 mmol), Co(O$_2$-CCH$_3$)$_2$·4H$_2$O (0.055 g, 0.221 mmol), bpy (0.068 g, 0.435 mmol), H$_2$PO$_3$(CH$_2$)$_3$PO$_3$H$_2$ (0.091 g, 0.446 mmol), H$_2$O (10 g, 555 mmol), and concentrated HF (0.125 g) in the mole ratio of 2.51:0.51:1:1: 1276 at 200 °C for 72 h produced red crystals of **12** suitable for X-ray diffraction in 53% yield (initial pH, 1.5; final pH, 1). IR (KBr pellet, cm^{-1}): 2917 (s), 1613 (w), 1540 (w), 1454 (w), 1417 (w), 1384 (w), 1249 (w), 1197 (m), 1115 (m), 1046 (s), 963 (m), 902 (s), 772 (m), 690 (s, br), 621 (m), 551 (m).

Synthesis of [Co(terpy)$_2$][Mo$_5$O$_{14}$(OH){O$_3$P(CH$_2$)$_3$PO$_3$}]·H$_2$O (13·H$_2$O). The reaction of MoO$_3$ (0.159 g, 1.105 mmol), Co(O$_2$-CCH$_3$)$_2$·4H$_2$O (0.110 g, 0.442 mmol), terpy (0.103 g, 0.442 mmol), H$_2$PO$_3$(CH$_2$)$_3$PO$_3$H$_2$ (0.090 g, 0.441 mmol), H$_2$O (10 g, 555 mmol),

and concentrated CH$_3$COOH (0.125 g) in the mole ratio of 2.5: 1.0:1.0:1.0:2551 at 200 °C for 72 h yielded yellow rods of **13**·H$_2$O in 64% yield that were suitable for X-ray diffraction (initial pH, 2.5; final pH, 2.0). IR (KBr pellet, cm^{-1}): 2970 (s, br), 2926 (s), 1588 (m), 1468 (w), 1401 (m), 1323 (w), 1244 (w), 1232 (w), 1142 (w), 1095 (m), 1089 (m), 1010 (m), 921 (s), 894 (s), 865 (s), 782 (s), 676 (s, br), 557 (m).

Synthesis of [{Co$_2$(phen)$_3$(H$_2$O)}Mo$_5$O$_{15}${O$_3$P(CH$_2$)$_3$PO$_3$}] (14). A mixture of MoO$_3$ (0.157 g, 1.091 mmol), Co(O$_2$CCH$_3$)$_2$· 4H$_2$O (0.056 g, 0.225 mmol), phen (0.080 g, 0.444 mmol), H$_2$-PO$_3$(CH$_2$)$_3$PO$_3$H$_2$ (0.091 g, 0.446 mmol), H$_2$O (10 g, 555 mmol), and concentrated HF (0.125 g) in the mole ratio of 2.5:0.51:1:1: 1250 was stirred briefly before being heated to 200 °C for 72 h. Orange platelike crystals of **13** were isolated in 42% yield (initial pH, 2.0; final pH, 1.5). IR (KBr pellet, cm^{-1}): 2921 (s), 1613 (m), 1540 (w), 1409 (w), 1307 (w), 1254 (w), 1205 (m), 1119 (s), 1082 (m), 1058 (m), 935 (s), 775 (m), 681 (s, br), 555 (m), 531 (m).

X-ray Crystallography. Structural measurements for **1**−**14** were performed on a Bruker-AXS SMART-CCD diffractometer at low temperature (90 K) using graphite-monochromated Mo Kα radiation

($\lambda_{Mo\ K\alpha}$ = 0.710 73 Å; Table 1)[50] The data were corrected for Lorentz and polarization effects and absorption using SADABS.[51a] The structures were solved by direct methods. All non-hydrogen atoms were refined anisotropically. After all of the non-hydrogen atoms were located, the models were refined against F^2 initially using isotropic and later anisotropic thermal displacement parameters. Hydrogen atoms of the organic components were introduced in calculated positions and refined isotropically. Hydrogen atom positions were not assigned to the water molecules of crystallization. Neutral atom scattering coefficients and anomalous dispersion corrections were taken from the *International Tables*, Vol. C.[52] All calculations were performed using SHELXTL crystallographic software packages.[51b]

Magnetism. The magnetic data were recorded on polycrystalline samples in the 2−300 K temperature range using a Quantum Design MPMS-5S SQUID spectrometer. Calibrating and operating procedures have been reported elsewhere.[53] The temperature-dependent magnetic data were obtained at a magnetic field of H = 1000 Oe, and the diamagnetic background from the sample holder was corrected.

Calculations. Model clusters of $\{Mo_5O_{15}(O_3PR)_2\}^{4-}$ with the alkyl chains reduced to methyl groups, $\{Mo_5O_{15}(O_3PCH_3)_2\}^{4-}$ were examined using density functional theory (DFT) methods. Gaussian 03[54] was used for the $\{Mo_5O_{15}(O_3PCH_3)_2\}^{4-}$ geometry optimization and charge analysis with the B3LYP hybrid density functional[55] program option "fine" integration grid size (corresponding to 75 radial shells and 302 angular points per shell), the 6-31+G(d) Gaussian-type basis sets for H, C, O, and P,[56] and the LANL2DZ effective core potential for Mo.[57] This level of theory is herein referred to as "B3LYP." DMol³ [58] was used for a $\{Mo_5O_{15}(O_3\text{-}PCH_3)_2\}^{4-}$ geometry optimization and charge analysis with the BLYP generalized gradient approximation density functional,[59] program option "fine" integration grid size (k-point separation of 0.04 Å^{-1}), and DND numerical basis set (comparable to a 6-31G-(d) Gaussian-type basis set) for all atoms.[60] This level of theory is referred to as "BLYP/DND". Efforts to employ DMol³ for a solid-state DFT (BLYP/DND) study of the crystal cell of $\{Mo_5O_{15}(O_3\text{-}PR)_2\}^{4-}$ were undertaken but, due to the computational requirements of this system, are left for subsequent study. Preliminary results are presented concerning the predicted positions of the hydrogen atoms and water orientations in the crystal cell at a BLYP/DN level of theory. All figures were generated with VMD[61] and POVRay.[62]

Results and Discussion

Syntheses and Infrared Spectroscopy. The combination of hydrothermal methods[63−69] with the introduction of organic ligands as tethers between single metal or metal cluster nodes has been routinely exploited in the preparation of structurally complex organic−inorganic hybrid materials.[70] In this case, the reactions of MoO_3, copper(II) acetate or copper(II) acetylacetonate (acac), tpyprz, the appropriate diphosphonic acid, a mineralizer such as acetic acid or HF, and water at 170−200 °C for 72−98 h provide crystalline samples of compounds **1−11** in modest to good yields. The reaction conditions reported provided optimal yields of the products and were determined by variations in stoichiometries, pH, and temperature.

It is noteworthy that relatively minor variations in reaction conditions can profoundly influence the identities of the products. This general observation is most obviously manifested in the four phases incorporating propylene diphosphonate as a component, **4−7**. Thus, increasing the ratios of MoO_3, $Co(O_2CCH_3) \cdot 4H_2O$, and diphosphonic acid to tpyprz used to prepare **4** provided compound **5** in good yield. Similarly, raising the reaction temperature from 180 °C, used in the preparations of **4** and **5**, to 200 °C resulted in the isolation of **6**. Finally, substituting $Co(acac)_2$ for $Co(O_2\text{-}CCH_3)_2 \cdot 4H_2O$ gave compound **7** in low yield.

The reaction pH is a critical determinant in the syntheses of these materials. Reasonable yields of crystalline product were obtained in the pH range of 2.0−4.0. Lower pH resulted in microcrystalline mixtures, while basic pH correlated with decomposition of the tpyprz ligand.

The infrared spectra of the complexes are characterized by two medium to strong bands in the 880−940 cm^{-1} range assigned to symmetric and antisymmetric $\nu(Mo=O)$ of the *cis* $\{MoO_2\}$ groups of the molybdate substructures. The medium to strong bands in the 650−770 cm^{-1} are attributed to $\nu(Mo-O-Mo)$. A series of three medium to strong intensity peaks in the 960−1200 range are associated with $\nu(P-O)$ bands of the diphosphonate ligands, while the series

(50) Bruker-AXS. *SMART Software*, Version 5.630; Siemens Analytical X-ray Instruments: Madison, WI, 1994.

(51) (a) Sheldrick, G. M. *SADABS: Program for Empirical Absorption Corrections*; University of Göttingen: Göttingen, Germany, 1996. (b) Sheldrick, G. M. *SHELXTL-Plus: Program for Refinement of Crystal Structures*; Version 6.14; Bruker-AXS: Madison, WI, 1996.

(52) *International Tables for Crystallography*; Prince, E., Ed.; Springer: Chester, UK, 2004; Vol. C.

(53) O'Connor, C. J. *Prog. Inorg. Chem.* **1979**, *29*, 203.

(54) Frisch, M. J.; Trucks, G. W.; Schlegel, H. B.; Scuseria, G. E.; Robb, M. A.; Cheeseman, J. R.; Montgomery, J. A., Jr.; Vreven, T.; Kudin, K. N.; Burant, J. C.; Millam, J. M.; Iyengar, S. S.; Tomasi, J.; Barone, V.; Mennucci, B.; Cossi, M.; Scalmani, G.; Rega, N.; Petersson, G. A.; Nakatsuji, H.; Hada, M.; Ehara, M.; Toyota, K.; Fukuda, R.; Hasegawa, J.; Ishida, M.; Nakajima, T.; Honda, Y.; Kitao, O.; Nakai, H.; Klene, M.; Li, X.; Knox, J. E.; Hratchian, H. P.; Cross, J. B.; Bakken, V.; Adamo, C.; Jaramillo, J.; Gomperts, R.; Stratmann, R. E.; Yazyev, O.; Austin, A. J.; Cammi, R.; Pomelli, C.; Ochterski, J. W.; Ayala, P. Y.; Morokuma, K.; Voth, G. A.; Salvador, P.; Dannenberg, J. J.; Zakrzewski, V. G.; Dapprich, S.; Daniels, A. D.; Strain, M. C.; Farkas, O.; Malick, D. K.; Rabuck, A. D.; Raghavachari, K.; Foresman, J. B.; Ortiz, J. V.; Cui, Q.; Baboul, A. G.; Clifford, S.; Cioslowski, J.; Stefanov, B. B.; Liu, G.; Liashenko, A.; Piskorz, P.; Komaromi, I.; Martin, R. L.; Fox, D. J.; Keith, T.; Al-Laham, M. A.; Peng, C. Y.; Nanayakkara, A.; Challacombe, M.; Gill, P. M. W.; Johnson, B.; Chen, W.; Wong, M. W.; Gonzalez, C.; and Pople, J. A. *Gaussian 03*, Revision C.02; Gaussian: Wallingford, CT, 2004.

(55) Becke, A. D. *J. Chem. Phys.* **1993**, *98*, 5648.

(56) H, C, O: Hehre, W. J.; Ditchfield, R.; Pople, J. A. *J. Chem. Phys.* **1972**, *56*, 2257. P: Francl, M. M.; Petro, W. J.; Hehre, W. J.; Binkley, J. S.; Gordon, M. S.; DeFrees, D. J.; Pople, J. A. *J. Chem. Phys.* **1982**, *77*, 3654.

(57) Hay, P. J.; Wadt, W. R. *J. Chem. Phys.* **1985**, *82*, 284.

(58) Delley, B. *J. Chem. Phys.* **1990**, *92*, 508.

(59) Becke, A. D. *Phys. Rev. A* **1988**, *38*, 3098, Lee, C.; Yang, W.; Parr, R. G. *Phys. Rev. B* **1988**, *37*, 785.

(60) Delley, B. *J. Chem. Phys.* **2000**, *113*, 7756.

(61) Humphrey, W.; Dalke, A.; Schulten, K. *J. Mol. Graphics* **1996**, *14*, 33.

(62) Persistence of Vision Raytracer (POV-Ray), v3.6, Persistence of Vision Raytracer Pty. Ltd., 2006.

(63) Stein, A.; Keller, S. W.; Mallouk, *Science* **1993**, *259*, 1558.

(64) Gopalakrishnan, J. *Chem. Mater.* **1995**, *7*, 1265.

(65) Whittinghan, M. S. *Curr. Opin. Solid State Mater. Sci.* **1996**, *1*, 227.

(66) Weller, M.; Dann, S. E. *Curr. Opin. Solid State Mater. Sci.* **1998**, *3*, 137.

(67) Gopalakrishnan, J.; Bhuvanrh, N. S. P.; Rangan, K. K. *Curr. Opin. Solid State Mater. Sci.* **1996**, *1*, 285.

(68) Yoshimura, M.; Suchanek, W. L.; Byrappa, K. *MRS Bull.* **2000**, *25*, 17.

(69) Fing, S.; Xu, R. *Acc. Chem. Res.* **2001**, *34*, 239.

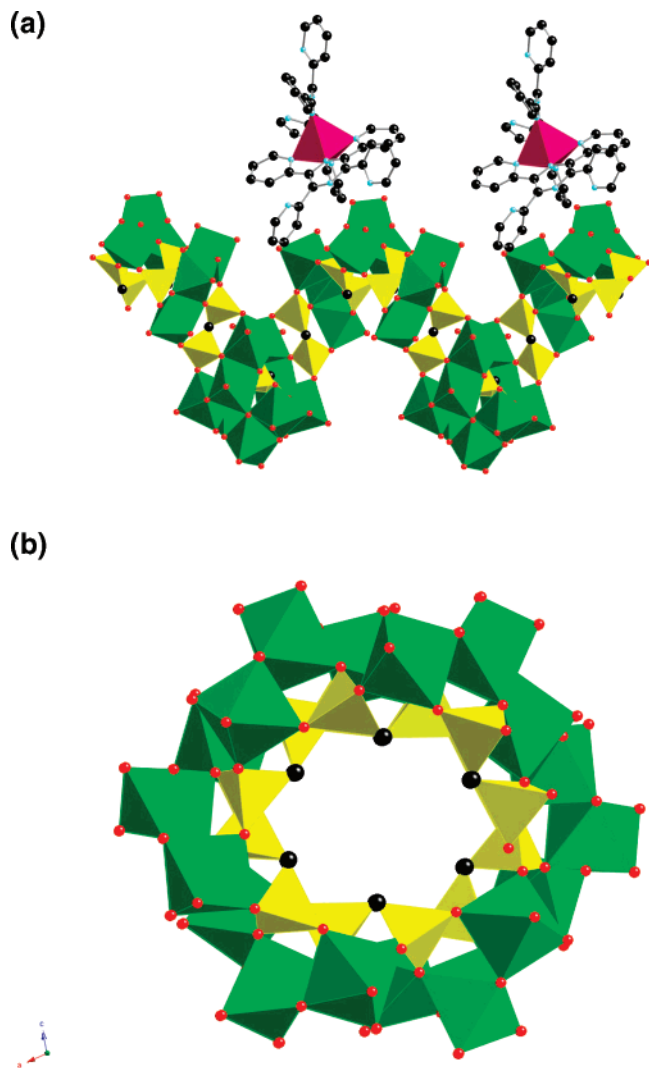(70) Zubieta, J. *Compr. Coord. Chem. II*, **2003**, *1*, 697.

(a)

(b)

Figure 1. (a) View of the one-dimensional phosphomolybdate chain and isolated $\{Co(H_3tpyprz)_2\}^{8+}$ cations of $[Co(H_3tpyprz)_2][(Mo_3O_9)_3(O_3PCH_2-PO_3)_3]\cdot 7H_2O\cdot C_5H_5N$ ($1\cdot 7H_2O\cdot py$); (b) the structure of the phosphomolybdate chain of **1** viewed parallel to the b-axis, showing the spiral profile of the chain.

of prominent bands in the $1400-1650$ cm^{-1} rang have been assigned to the tpyprz ligand.

X-ray Structures. In common with the previously reported oxomolybdate−organodiphosphonate/M(II)−tpyprz families where M(II) = Cu(II) and Ni(II), the chemistry of the oxomolybdate−organodiphosphonate/Co(II)−tpyprz compounds of this study exhibits considerable structural diversity, manifested in one-, two-, and three-dimensional phases. It is noteworthy that while the Cu(II)-based class exhibited exclusively the binuclear $\{Cu_2(tpyprz)(H_2O)_x\}^{4+}$ subunit as the cationic component, the different coordination preferences of Ni(II) were reflected in oligomeric or one-dimensional $\{Ni_x(tpyprz)_y\}_n^{2xn+}$ building blocks. Similarly, the Co(II)-based materials of this study exhibit catenation of the cationic substructure, resulting in $\{CoN_6\}$ cores as well as $\{CoN_3O_3\}$ coordination polyhedra.

(a) $[Co(H_2tpyprz)_2][(Mo_3O_8)_3(O_3PCH_2PO_3)_3]\cdot 7H_2O\cdot C_5H_5N$. As shown in Figure 1a, the structure of $[Co(H_2-tpyprz)_2][(Mo_3O_8)_3(O_3PCH_2PO_3)_3]\cdot 7H_2O\cdot C_5H_5N$ ($1\cdot 7H_2O\cdot py$) consists of discrete $\{Mo_3O_8(O_3PCH_2PO_3)\}_n^{2n-}$ spirals and

isolated $\{Co(H_2tpyprz)_2\}^{6+}$ charge compensating cations. The phosphomolybdate substructure is constructed from triads of edge-sharing $\{MoO_6\}$ octahedra linked through $\{O_3PCH_2-PO_3\}^{4-}$ ligands into a one-dimensional spiral. The central molybdenum site of the trinuclear cluster shares cis-edges with the two peripheral sites and exhibits two bridging oxo-groups, two terminal oxo-groups, and two oxygen donors from two adjacent diphosphonate ligands. The geometry of the peripheral molybdenum sites is defined by two cis-terminal oxo-groups, a bridging oxo-group to the central molybdenum site, and three oxygen donors from two adjacent diphosphonate ligands.

Each methylenediphosphonate ligand serves to bridge two adjacent molybdenum triads of the chain. One phosphorus terminus contributes an oxygen donor to a peripheral molybdenum site and another as a bridge between the peripheral and central molybdenum sites of a triad, while the second phosphorus group of the diphosphonate links to the other peripheral molybdenum site of this trinuclear unit. Thus, the diphosphonate ligand chelates to one molybdenum site, forming a six-membered $\{Mo-O-P-C-P-O-\}$ ring. The remaining oxygen atoms of the diphosphonate ligand bridge to the adjacent molybdenum cluster of the chain with the oxygen donors of one phosphorus site linking to two molybdenum sites while the single remaining oxygen donor of the second phosphorus site coordinates to the remaining molybdenum site of the triad. The polyhedral connectivity produces a distinctive spiral to the phosphomolybdate chain, such that, when viewed along the chain axis (crystallographic b direction), the structural profile appears circular with an inner diameter of 6.10 Å.

It is noteworthy that $1\cdot 7H_2O\cdot py$ provides an unusual example of a phosphomolybdate chain of this general class which is not decorated with covalently attached secondary metal−ligand subunits. Furthermore, the tpyprz ligand is not present in its customary role of binucleating ligand, but rather coordinates through one terminus, consisting of two pyridyl nitrogens and a pyrazine nitrogen, while the remaining nitrogen sites are protonated. The Co(II) site exhibits distorted octahedral $\{CoN_6\}$ geometry through coordination to two tpyprz ligands. Consequently, the cationic subunit contains two triply protonated tpyprz ligands to provide the necessary charge compensation as the $[Co(H_3tpyprz)_2]^{8+}$ subunit.

The structure of **1** once again illustrates the structure-directing influence of the diphosphonate ligand geometry, in particular the tether length. The recurring molecular building block for this class of oxomolybdenum−diphosphonates is the pentanuclear cluster $\{Mo_5O_{15}(O_3PR)_2\}^{4-}$, as noted in Table 2. However, other $\{Mo_xO_y(O_3ER)_z\}^{n-}$ building blocks have been observed, most notably $\{Mo_6O_{18}(O_3AsR)_2\}^{4-}$ when the organophosphonate is replaced by organoarsonate and the $\{(Mo_3O_8)_x(O_3PCH_2PO_3)_y\}_n^{n-}$ building blocks which occur regularly for the phases incorporating methylene-diphosphonate as ligand. It is apparent that the absence of the $\{Mo_5O_{15}(O_3PR)_2\}^{4-}$ building unit in the methylene-diphosphonate materials reflects the steric constraints imposed by the short tether length of the methylenediphospho-

Cobalt−Molybdophosphonate Hybrid Materials

Table 2. Summary of Selected Structural Characteristics of Materials Containing the $\{Mo_5O_{15}(O_3PR)_2\}^{4-}$ Subunit

compound	overall dimensionality	M(II) attachments per cluster	attachment type	clusters linked per cationic unit
$[\{Cu_2(phen)_3(H_2O)_2\}Mo_5O_{15}\{O_3P(CH_2)_3PO_3\}]$	1D	2	$2 \times \{Mo=O\}$	
$[Co(bpy)_3]_2[Mo_5O_{15}\{O_3P(CH_2)_3PO_3\}]$	1D	0	-	
$[\{Co_2(phen)_3(H_2O)\}Mo_5O_{15}\{O_3P(CH_2)_3PO_3\}]$	1D	5	$3 \times \{Mo=O\}$ $2 \times \{P-O-Mo\}$	2
$[\{Cu_2(bpy)_3(H_2O)\}Mo_5O_{15}\{O_3P(CH_2)_4PO_3\}]$	1D	3	$2 \times \{Mo=O\}$ $1 \times \{P-O-Mo\}$	
$[\{Cu(terpy)(H_2O)\}_2Mo_5O_{15}\{O_3P(CH_2)_2PO_3\}]$	1D	2	$2 \times \{Mo=O\}$	
$[\{Co(H_2(tpyprz)\}Mo_5O_{15}(O_3PCH_2CH_2PO_3)]$	1D	3	$2 \times \{Mo=O\}$ $1 \times \{P-O-Mo\}$	2
$[\{Cu(terpy)\}_2Mo_5O_{15}\{O_3P(CH_2)_3PO_3\}]$	2D	4	$2 \times \{Mo=O\}$ $2 \times \{Mo-O-Mo\}$	2
$[\{Cu_2(tpyprz)(H_2O)_2\}Mo_5O_{15}\{O_3P(CH_2)_2PO_3\}]$	2D	3	$2 \times \{Mo=O\}$ $1 \times \{P-O-Mo\}$	3
$[\{Ni_4(tpyprz)_3\}Mo_5O_{15}\{O_3P(CH_2)_2PO_3\}]$	2D	3	$2 \times \{Mo=O\}$ $1 \times \{P-O-Mo\}$	4
$[\{Co_4(tpypry)_3\}Mo_5O_{15}\{O_3P(CH_2)_2PO_3\}]\cdot18H_2O$	2D	3	$2 \times \{Mo=O\}$ $1 \times \{P-O-Mo\}$	4
$[\{Cu_2(tpyprz)(H_2O)_2\}Mo_5O_{15}\{O_3P(CH_2)_3PO_3\}]$	3D	4	$4 \times \{Mo=O\}$	3
$[\{Ni_2(tpyprz)(H_2O)_3\}Mo_5O_{15}\{O_3P(CH_2)_3PO_3\}]$	3D	4 and 2	$4 \times \{Mo=O\}$ $2 \times \{Mo=O\}$	4 2
$[\{Ni_3(tpypry)_2(H_2O)_2\}(Mo_5O_{15})(Mo_2F_2O_4)\{O_3P(CH_2)_3PO_3\}]$	2D	4	$2 \times \{Mo=O\}$ $2 \times \{P=O\}$	4
$[\{Co_2(tpyprz)_2Mo_5O_{15}\{O_3P(CH_2)_3O_3\}]\cdot5H_2O$	1D	3	$2 \times \{Mo=O]$ $1 \times \{P-O-Mo\}$	2
$[\{Co_2(tpyprz)(H_2O)_3\}Mo_5O_{15}\{O_3P(CH_2)_3PO_3\}]\cdot H_2O$	3D	4 and 2	$4 \times \{Mo=O\}$ $2 \times \{Mo=O\}$	4 2
$[\{Co_2(tpyprz)(H_2O)_3\}Mo_5O_{15}\{O_3P(CH_2)_3PO_3\}]\cdot7H_2O$	3D	3	$3 \times \{Mo=O\}$	3
$(H_3O)_2[\{Co_3(tpyprz)_2(H_2O)_3\}(Mo_5O_{15}\{O_3P(CH_2)_3PO_3\})_2)]\cdot21.4H_2O$	3D	2	$2 \times \{Mo=O\}$	2
$[\{Cu_2(tpyprz)(H_2O)_2\}Mo_5O_{15}\{O_3P(CH_2)_4PO_3\}]\cdot H_2O$	3D	4	$4 \times \{Mo=O\}$	3
$[\{Ni_2(tpyprz)_2\}Mo_5O_{15}\{O_3P(CH_2)_4PO_3\}]$	1D	3	$2 \times \{Mo=O\}$ $1 \times \{P-O-Mo\}$	2
$[\{Ni_2(tpyprz)(H_2O)_2\}Mo_5O_{15}\{O_3P(CH_2)_4PO_3\}]$	3D	4	$4 \times \{Mo=O\}$	4
$[\{Co_2(tpyprz)(H_2O)_2\}Mo_5O_{15}\{O_3P(CH_2)_4PO_3\}]\cdot2H_2O$	3D	4	$4 \times \{Mo=O\}$	4
$[\{Co_2(tpyprz)(H_2O)_3\}Mo_5O_{15}\{O_3P(CH_2)_5PO_3\}]$	3D	3	$3 \times \{Mo=O\}$	3
$[\{Co_2(tpyprz)(H_2O)_3\}Mo_5O_{15}\{O_3P(CH_2)_9PO_3\}]\cdot2.5H_2O$	2D	3	$3 \times \{Mo=O\}$	3

nate ligand. Diphosphonate ligands $\{O_3P(CH_2)_nPO_3\}^{4-}$ with $n \geq 2$ possess sufficient spatial extension to bridge cluster building blocks, thus favoring self-assembly and incorporation of the robust pentamolybdate core. In contrast, methylenediphosphonate is constrained by the short tether length to adopt chelation through oxygen donors at either phosphorus site as the preferred ligation mode, which would preclude formation of the $\{Mo_5O_{15}(O_3PR)_2\}^{4-}$ cluster building block.

It is also curious that the structure of **1** is quite distinct from those of previously reported examples of oxomolybdate−methylenediphosphonate/M(II)−tpyprz phases, although these are also constructed from the recurrent $\{Mo_3O_8\}$ cluster building block. Thus, $[\{Cu_2(tpyprz)(H_2O)\}Mo_3O_8(HO_3PCH_2PO_3)_2]$ consists of $[Mo_3O_8(HO_3PCH_2PO_3)_2]^{4-}$ clusters linked through $\{Cu_2(tpyprz)(H_2O)\}^{4+}$ subunits into a chain. While $[\{Cu_2(tpyprz)(H_2O)\}_2(Mo_3O_8)_2(O_3PCH_2PO_3)_3]$ is also one-dimensional, the chain is constructed from $\{(Mo_3O_8)_2(O_3PCH_2PO_3)_3\}^{8-}$ molecular clusters, consisting of a pair of-$\{Mo_3O_8\}$ triads linked through the diphosphonate ligands, which are in turn linked through the secondary metal−ligand subunits $\{Cu_2(tpyprz)(H_2O)\}^{4+}$. On the other hand, the structures $[\{M_2(tpyprz)(H_2O)_2\}(Mo_3O_8)_2(O_3PCH_2PO_3)_2]$ (M = Ni, Cu) are similar to that of **1**, since these also exhibit one-dimensional $\{Mo_3O_8(O_3PCH_2PO_3)\}_n^{4n-}$ substructures. However, for these Ni(II) and Cu(II) derivatives, the phosphomolybdate chains are linked through the $\{M_2(tpyprz)(H_2O)\}^{4+}$ subunits into a three-dimensional framework.

Furthermore, the detailed connectivity within the $\{Mo_3O_8(O_3PCH_2PO_3)\}_n^{4n-}$ chains is quite distinct. For the Ni(II) and Cu(II) analogues, each diphosphonate bridges three neighboring molybdate triads, rather than two as adopted in the case of **1**.

(b) $[\{Co_4(tpyprz)_3\}(Mo_5O_{15})_2(O_3PCH_2CH_2PO_3)_2]\cdot18H_2O$. Increasing the diphosphonate tether length provides a material incorporating the common $\{Mo_5O_{15}(O_3PR)_2\}^{4-}$ building block. The two-dimensional structure of $[\{Co_4(tpyprz)_3\}(Mo_5O_{15})_2 (O_3PCH_2CH_2PO_3)_2]\cdot18H_2O$ (**2**·18H_2O), shown in Figure 2a, is constructed from $\{Mo_5O_{15}(O_3PCH_2CH_2PO_3)\}_n^{4n-}$ chains linked through tetranuclear $\{Co_4(tpyprz)_3\}^{8+}$ cationic subunits. The molybdophosphonate substructure consists of the commonly observed pentamolybdate $\{Mo_5O_{15}(O_3PR)_2\}^{4-}$ clusters linked through the ethylene tethers of the diphosphonate ligand. The cationic cluster exhibits two Co(II) environments. The two interior Co(II) sites of the chain enjoy $\{CoN_6\}$ coordination defined by two pyridyl nitrogen and one pyrazine nitrogen donors from each of two tpyprz ligands. The terminal Co(II) sites of the chain possess $\{CoN_3O_3\}$ coordination through bonding to the remaining nitrogen donors of the tpyprz ligands, two terminal $\{Mo=O\}$ oxo-groups from two adjacent clusters of a chain, and one phosphonate $\{P-O-Mo\}$ oxygen atom. Each $\{Co_4(tpyprz)_3\}^{8+}$ chain bridges two adjacent phosphomolybdate chains of the 2-D network. The connectivity pattern produces a distinct ruffling of the network, as shown in Figure 2b. The sinusoidal profile is defined by an amplitude of 15.1 Å
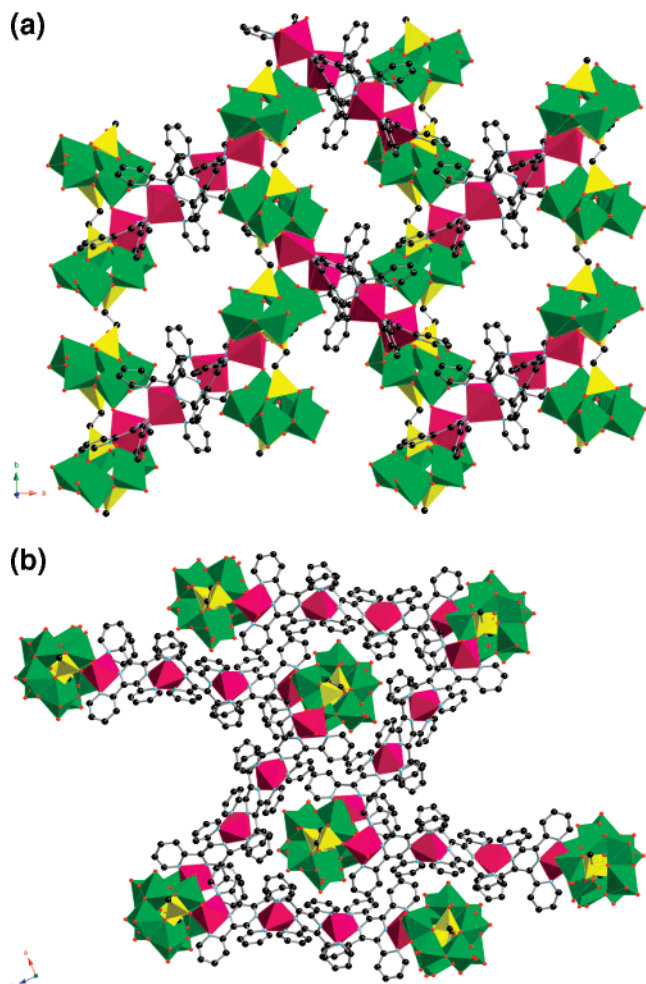
Figure 2. (a) Two-dimensional structure of [{Co$_4$(tpyprz)$_3$}(Mo$_5$O$_{15}$)$_2$(O$_3$-PCH$_2$CH$_2$PO$_3$)$_2$]·18H$_2$O (**2**·18H$_2$O) in the *ab* plane; (b) stacking of adjacent folded layers of **2**, viewed in the *ac* plane.

Figure 3. (a) View of the chain structure of [{Co(H$_2$tpyprz)}Mo$_5$O$_{15}$(O$_3$-PCH$_2$CH$_2$PO$_3$)] (**3**); (b) view of the structure looking down the chains (parallel to the crystallographic *a*-axis) of four adjacent chains.

and a period of 24.2 Å. The water molecules of crystallization reside in the interlamellar domain.

(c) Propylenediphosphonate Derivatives. Under modified reaction conditions, a second ethylenediphosphonate phase [{Co(H$_2$tpyprz)}Mo$_5$O$_{15}$(O$_3$PCH$_2$CH$_2$PO$_3$)] (**3**) is isolated. As shown in Figure 3, the structure of **3** consists of one-dimensional {Mo$_5$O$_{15}$(O$_3$PCH$_2$CH$_2$PO$_3$)}$_n^{4n-}$ chains decorated with {Co(H$_2$tpyprz)}$^{4+}$ subunits. The phosphomolybdate substructure is unexceptional and displays the common {Mo$_5$O$_{15}$(O$_3$PR)$_2$}$^{4-}$ building blocks, linked through the diphosphonate tether groups.

The Co(II) sites exhibit distorted octahedral {CoO$_3$N$_3$} coordination, through bonding to two pyridyl nitrogens and a pyrazine nitrogen of a tpyprz ligand, a terminal molybdenum oxo-group, and a phosphonate oxygen donor of one phosphomolybdate ring and a terminal oxo-group of a second phosphomolybdate ring. Thus, each Co(II) center bridges two adjacent {Mo$_5$O$_{15}$(O$_3$PR)$_2$}$^{4-}$ units of the chain.

It is noteworthy that a single dipyridyl/pyrazine nitrogen terminus of the tpyprz ligand is involved in metal coordination. The second terminus of the ligand projects outward at an angle of 41° with respect to the axis of the phosphomolybdate chain. Charge balance requirements dictate that this second terminus is doubly protonated. The final Fourier maps
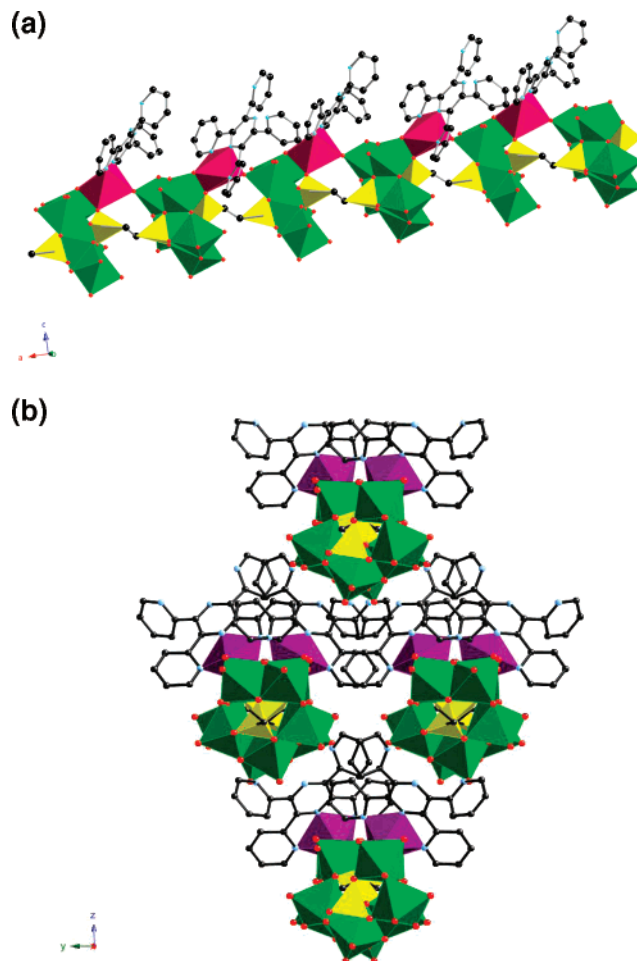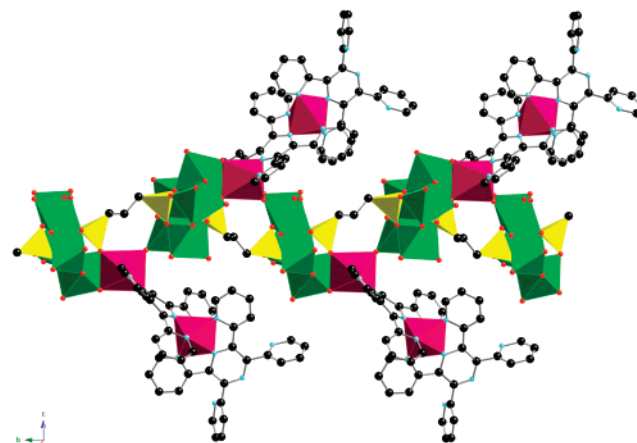
Figure 4. View of the one-dimensional structure of [{Co$_2$(tpyprz)$_2$}-Mo$_5$O$_{15}${O$_3$P(CH$_2$)$_3$PO$_3$}]·5H$_2$O (**4**·5H$_2$O).

indicated that the pyridyl nitrogen positions are the protonation sites.

The consequences of variations in hydrothermal reaction conditions on structure are illustrated by phases **4**−**7**. As shown in Figure 4, the structure of [{Co$_2$(tpyprz)$_2$}Mo$_5$O$_{15}$-{O$_3$P(CH$_2$)$_3$PO$_3$}]·5H$_2$O (**4**·5H$_2$O) is one-dimensional. The structure may be described as the common [Mo$_5$O$_{15}${O$_3$P-(CH$_2$)$_3$PO$_3$}]$_n^{4n-}$ chain decorated with {Co$_2$(tpyprz)$_2$}$^{4+}$
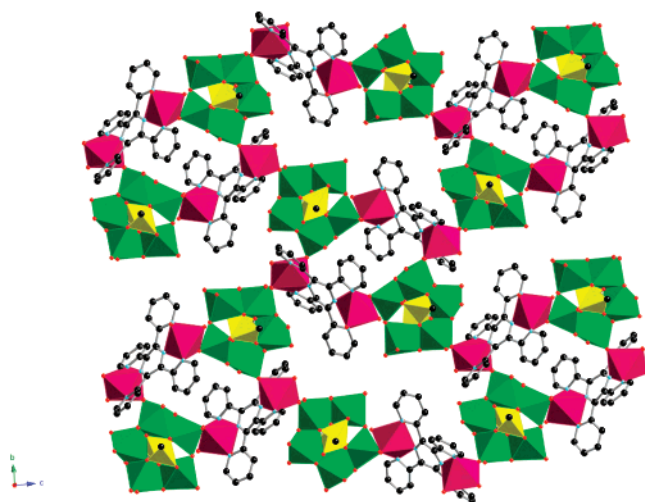
Figure 5. View of the three-dimensional structure of [{Co₂(tpyprz)-(H₂O)₃}Mo₅O₁₅{O₃P(CH₂)₃PO₃}]·7H₂O (**5**·7H₂O) in the *bc* plane, showing the bimetallic cobalt phosphomolybdate layers.

subunits. The unusual feature of this structure is the presence of the pendant, rather than bridging, {Co₂(tpyprz)₂}⁴⁺ clusters, as a consequence of one Co(II) site having its coordination requirements satisfied by the second tpyprz ligand. Consequently, one Co(II) site of the binuclear cationic subunit exhibits {CoN₃O₃} coordination, with the bonding defined by the three nitrogen donors of a tpyprz ligand, a terminal oxo-group of a molybdenum site of a pentamolybdate cluster of the chain, and a terminal oxo-group and a bridging phosphonate oxygen {Mo−O(P)−Co} of a molybdenum site of a neighboring cluster of the chain. Thus, the Co(II) center shares a corner with a molybdenum of one cluster and an edge with the molybdenum site of a second cluster. The second Co(II) site exhibits {CoN₆} coordination through bonding to three nitrogen donors from each of two tpyprz ligands. The terminal tpyprz of the cationic grouping project two pendant pyridyl groups into the interchain domain.

The structure of **4** is analogous to that of the Ni(II) counterpart [{Ni₂(tpyprz)₂}Mo₅O₁₅{O₃P(CH₂)₄PO₃}]. Curiously, there is no analogous Ni(II) structure with a propylene tether in the diphosphonate ligand. The structure of **4** is also similar to that of **3**. However, charge balance is achieved in **4** by replacing the protonation sites of the {Co(H₂tpyprz)}⁴⁺ subunit with {Co(tpyprz)}²⁺ groups to provide the {Co₂-(tpyprz)₂}⁴⁺ moiety.

The remaining structures of the propylenediphosphonate subset of the oxomolybdate−diphosphonate/Co(II)−tpyprz family are three-dimensional. The structure of [{Co₂(tpyprz)-(H₂O)₃}Mo₅O₁₅{O₃P(CH₂)₃PO₃}]·7H₂O (**5**·7H₂O), shown in Figure 5, consists of [Mo₅O₁₅{O₃P(CH₂)₃PO₃}]ₙ⁴ⁿ⁻ chains linked through {Co₂(tpyprz)(H₂O)₃}⁴⁺ rods into a three-dimensional framework. The structure may be described as bimetallic cobalt phosphomolybdate layers parallel to the *bc* plane, cross-lined through propylene tethers of the diphosphonate ligand into a pattern with overall three-dimensional covalent connectivity. There are two distinct Co(II) environments of the general type {CoN₃O₃}. The first bonds to three nitrogen donors of the tpyprz ligand, an aqua group and
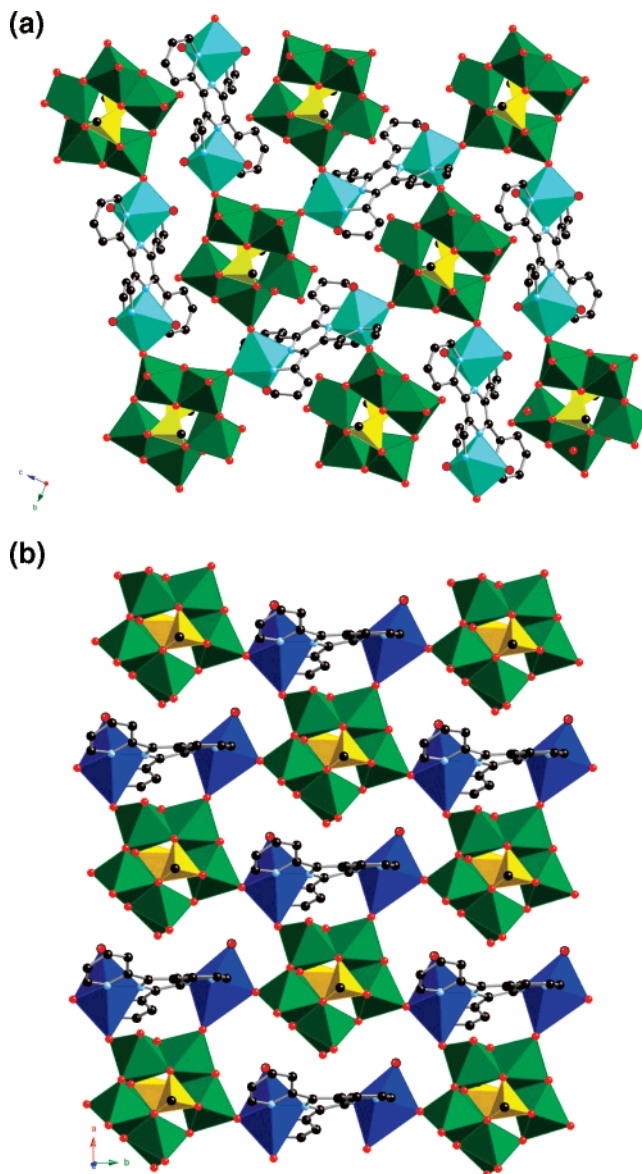

Figure 6. (a) Polyhedral representation of the structure of [{Ni₂(tpyprz)-(H₂O)₃}Mo₅O₁₅{O₃P(CH₂)₃PO₃}]; (b) view of the structure of [{Cu₂-(tpyprz)(H₂O)}Mo₅O₁₅{O₃P(CH₂)₃PO₃}]. Color scheme: as above with Ni, light blue octahedra, and Cu, dark blue polyhedra.

terminal oxo-groups from phosphomolybdate clusters of two neighboring chains. The second Co(II) site is bonded to three nitrogen donors of the tpyprz, two aqua ligands and a terminal oxo-group from a cluster of a third phosphomolybdate chain. Thus, each cationic rod cross-links three phosphomolybdate chains.

While the structure of **5** is reminiscent of [{Ni₂(tpyprz)-(H₂O)₃}Mo₅O₁₅{O₃P(CH₂)₃PO₃}] and [{Cu₂(tpyprz)(H₂O)}-Mo₅O₁₅{O₃P(CH₂)₃PO₃}], the three structures exhibit different detailed connectivities and aqua coordination modes. In contrast to **5**, the Ni(II) analogue has two discrete cationic subunits {Ni₂(tpyprz)(H₂O)ₙ}⁴⁺, *n* = 2 and 4, the former bridging clusters of four neighboring phosphomolybdate chains and the latter linking two chains (Figure 6). In the case of the Cu(II)-based material, each {Cu₂(tpyprz)-(H₂O)₂}⁴⁺ rod links three adjacent phosphomolybdate chains but through four points of connection. The major conse-

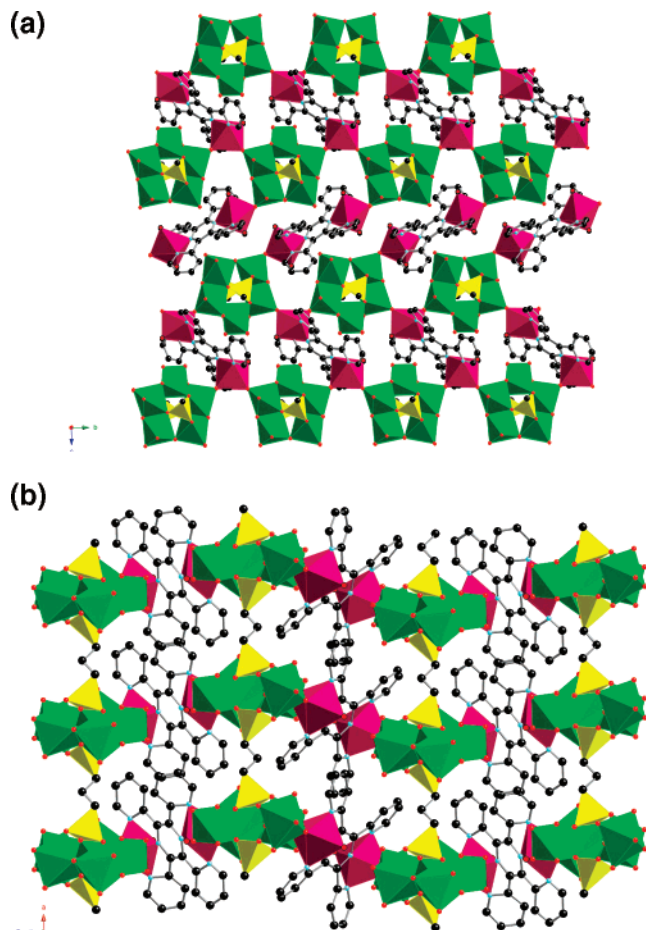**Figure 7.** (a) Three-dimensional structure of [{Co$_2$(tpyprz)(H$_2$O)$_3$}Mo$_5$O$_{15}$-{O$_3$P(CH$_2$)$_3$PO$_3$}]·H$_2$O (**6**·H$_2$O), viewed in the *bc* plane and showing the cobalt phosphomolybdate layer; (b) stacking of layers in **6** through the propylene bridges of the diphosphonate ligands.

quence of the different connectivity patterns and aqua ligation modes of the Co(II), Ni(II), and Cu(II) derivatives is the generation of considerably different void volumes in the three structures, a feature manifested in the different amounts of water of crystallization incorporated into the structures. Thus, the Ni(II) and Cu(II) structures exhibit relatively dense packing of the secondary metal−phosphomolybdate layers, with the cationic rods inserted into the intralamellar spaces between the phosphomolybdate clusters. Consequently, the Ni(II) structure exhibits one water of crystallization per formula unit and the Cu(II) analogue two water molecules. In contrast, the Co(II) structure possesses intralamellar cavities of approximate dimensions 4.10 × 15.6 Å and accommodates seven water molecules per formula unit.

As shown in Figure 7, the three-dimensional structure of [{Co$_2$(tpyprz)(H$_2$O)$_3$}Mo$_5$O$_{15}${O$_3$P(CH$_2$)$_3$PO$_3$}]·H$_2$O (**6**·H$_2$O) is also constructed of bimetallic cobalt molybdophosphonate layers linked through the propylene tethers of the diphosphonate ligands. The detailed connectivity between the cationic rods and the phosphomolybdate chains is distinct from that observed for **5** and identical to that of the Ni(II) analogue [{Ni$_2$(tpyprz)(H$_2$O)$_3$}Mo$_5$O$_{15}${O$_3$P(CH$_2$)$_3$PO$_3$}]. Thus, there are two unique {Co$_2$(tpyprz)(H$_2$O)$_n$}$^{4+}$ units with $n =$ 2 and 4. The cationic subunit with $n = 2$ bridges four neighboring [Mo$_5$O$_{15}${O$_3$P(CH$_2$)$_3$PO$_3$}]$_n^{4n−}$ chains. Each Co-

(II) site coordinates to three nitrogen donors of the tpyprz ligand, an aqua ligand, and terminal oxo-groups from two adjacent chains. When $n = 4$, each cationic subunit links two phosphomolybdate chains. The coordination at each cobalt site is defined by three nitrogen donors, two *trans*-aqua ligands and a terminal {Mo=O} oxo-group. The connectivity pattern of **5** reduces the available void volume with respect to that of **5**, an observation reflected in the relative amounts of water of crystallization incorporated in the structures: 1 per formula unit in **6** and 7 in **5**.

The final phase with propylenediphosphonate as linker is the open-framework material [H$_3$O]$_2$[{Co$_3$(tpyprz)$_2$(H$_2$O)$_3$}-(Mo$_5$O$_{15}$)$_2${O$_3$P(CH$_2$)$_3$PO$_3$}$_2$]·21.4H$_2$O (**7**·21.4H$_2$O). As shown in Figure 8, the complex 3-D structure of **7** is constructed from the recurrent [Mo$_5$O$_{15}${O$_3$P(CH$_2$)$_n$PO$_3$}]$_n^{4n−}$ chains ($n = 3$) cross-linked through {Co$_3$(tpyprz)$_2$(H$_2$O)$_3$}$^{6+}$ rods. While **7** shares with the structure of **2** the catenation of the Co(II)−tpyprz subunit, in this case a trinuclear cationic building block is observed. The central Co site exhibits {CoN$_6$} geometry through bonding to the tridentate termini of two tpyprz ligands. The {CoO$_3$N$_3$} geometries of the peripheral Co sites consist of the remaining three nitrogen donors of a tpyprz, two aqua ligands and a terminal oxo-group of a phosphomolybdate chain at one terminus, and of three nitrogen donors, one aqua ligand and two terminal oxo-groups from molybdenum sites of adjacent chains at the second terminus.

Since each cationic rod provides a total of only three attachment loci and the ratio of rods to cluster sites is 1:2, there is a low density of cross-linking attachments between the anionic chains and the cationic rods. As shown in Figure 8b, along a given chain, there is observed an alternating pattern of one and two vertex-sharing between phosphomolybdate clusters of the chain and cationic rods. Typically, each {Mo$_5$O$_{15}$(O$_3$PR)$_2$}$^{4−}$ cluster of the chain in structures constructed from this building block exhibits three or four attachment points. However, since the attachment points in **7** are staggered along the chain, each chain is linked to six adjacent chains, albeit in a rather open arrangement. This feature of the structure is reflected in the large open galleries of approximate dimensions 21.6 Å × 14.6 Å × 10.6 Å, running normal to the *bc* plane. The large amount of water crystallization, ca. 21.4H$_2$O per formula unit or 28.6% accessible volume per unit cell, is consistent with this observation.

While the Ni(II) and Co(II) analogues [{M$_4$(tpyprz)$_3$}-(Mo$_5$O$_{15}$)$_2$(O$_3$PCH$_2$CH$_2$PO$_3$)$_2$] are isomorphous, there is no Ni(II) structure analogous to that of **7**. Similarly, while a trinuclear cation is observed for [{Ni$_3$(tpyprz)$_2$(H$_2$O)$_2$}-(Mo$_5$O$_{15}$)(Mo$_2$F$_2$O$_4$){O$_3$P(CH$_2$)$_3$PO$_3$}$_2$], the structure of this material is two-dimensional and unrelated to that of **7**.

(d) [{Co$_2$(tpyprz)(H$_2$O)$_2$}Mo$_5$O$_{15}${O$_3$P(CH$_2$)$_4$PO$_3$}]·2H$_2$O. The compound incorporating butylene−diphosphonate could only be isolated at high temperature and is isomorphous with the analogues Ni(II) material. As shown in Figure 9, the structure of [{Co$_2$(tpyprz)(H$_2$O)$_2$}Mo$_5$O$_{15}${O$_3$P(CH$_2$)$_4$PO$_3$}]·2H$_2$O (**8**·2H$_2$O) is constructed from the common building blocks, {Mo$_5$O$_{15}$(O$_3$PR)$_2$}$_n^{4n−}$ chains and {Co$_2$(tpyprz)-

(a)

(b)

(c)
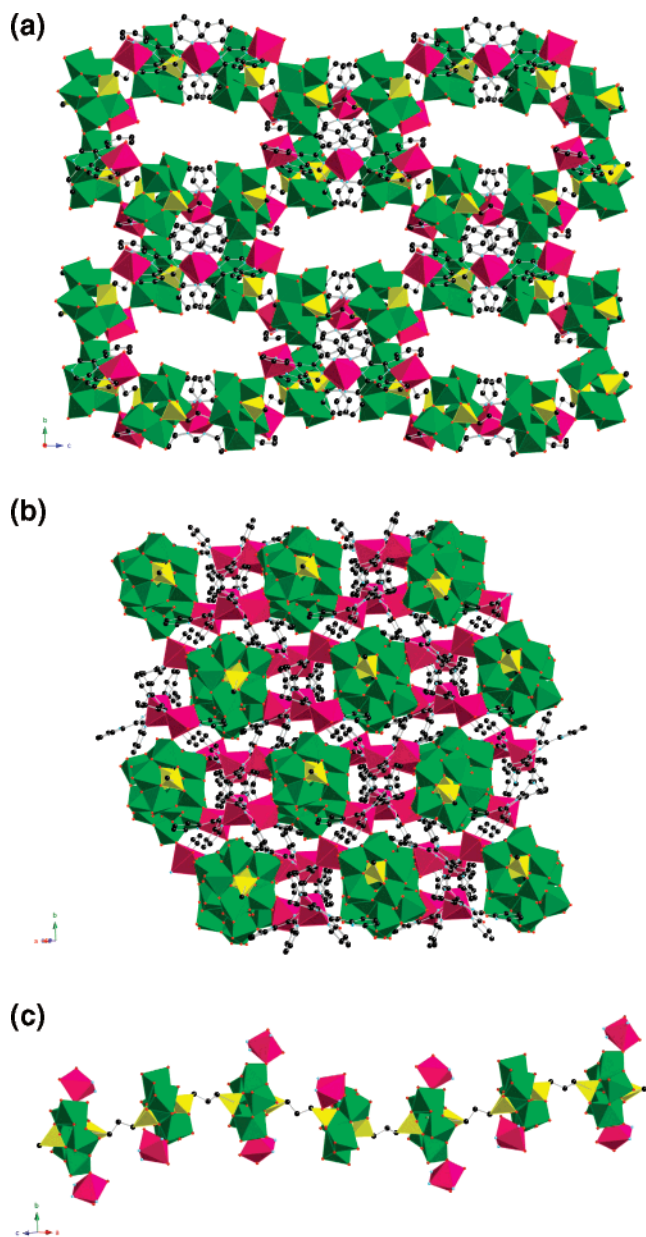
Figure 8. (a) Polyhedral view of the structure of [H$_3$O]$_2$[{Co$_3$(tpyprz)$_2$-(H$_2$O)$_3$}{Mo$_5$O$_{15}$}$_2${O$_3$P(CH$_2$)$_3$PO$_3$}$_2$]·21·4H$_2$O (**7**·21.4H$_2$O) in the *bc* plane; (b) view of the structure in the *ab* plane, looking down the [Mo$_5$O$_{15}${O$_3$P(CH$_2$)$_3$PO$_3$}]$_n^{4n-}$ chain axes; (c) polyhedral view of the phosphomolybdate chains of **7**, illustrating the association with one or two cobalt sites at alternating phosphomolybdate rings.

(H$_2$O)$_2$}$^{2+}$ rods. The structure may be described as bimetallic cobalt molybdophosphonate sheets in the *bc* plane. However, in addition to the two Co−O−Mo interactions of Figure 9a, each phosphomolybdate cluster is linked to two additional rods, as shown in Figure 9b. The rods projecting from the chains are staggered along the chain axis, such that each chain is linked to eight adjacent chains, as illustrated in Figure 9c.

A curious feature of the structure is the juxtaposition of attachment points at each cluster of the anionic chain. The four rods linked to the chain share vertices with three adjacent Mo sites, such that the central site shares two vertices with cobalt octahedra. The connectivity pattern produces little void
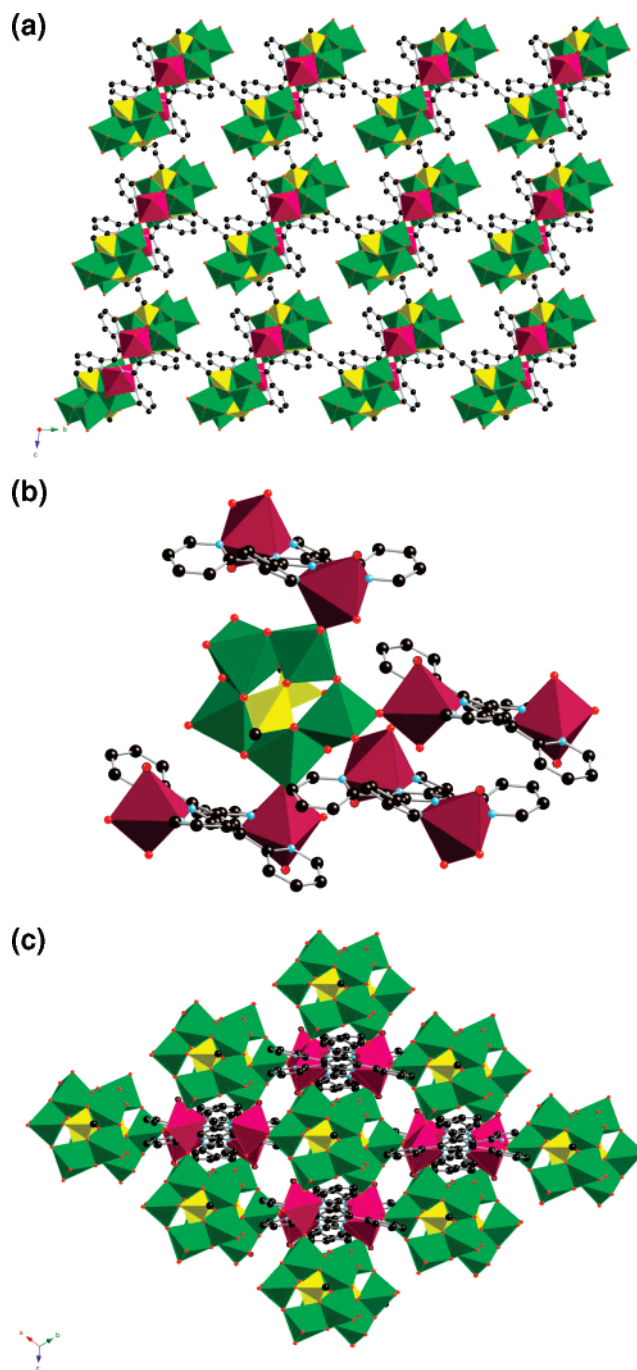
(a)

(b)

(c)

Figure 9. (a) Polyhedral view in the *ac* plane of a cobalt phosphomolybdate layer of the three-dimensional structure of [{Co$_2$(tpyprz)(H$_2$O)$_2$}-Mo$_5$O$_{15}${O$_3$P(CH$_2$)$_4$PO$_3$}]·2H$_2$O (**8**·2H$_2$O); (b) linking of each individual cluster to Co(II) sites; (c) linking of phosphomolybdate chains through {Co$_2$-(tpyprz)(H$_2$O)$_2$}$^{4+}$ rods into a three-dimensional framework.

volume as reflected in the amount of water of crystallization incorporated and the accessible void volume of 3.4%.

(e) Pentyldiphosphonate Derivatives. While the pentyl derivative [{Co$_2$(tpyprz)(H$_2$O)$_3$}Mo$_5$O$_{15}${O$_3$P(CH$_2$)$_5$PO$_3$}]·2.5H$_2$O (**9**·2.5H$_2$O) is also three-dimensional and constructed from {Mo$_5$O$_{15}$(O$_3$PR)$_2$}$_n^{4n-}$ chains and cationic rods in an analogous fashion to compounds **5** and **6**, the details of the connectivities between component buildings are quite distinct, as illustrated in Figure 10. When viewed in the *ac* plane, the simple network of {Mo$_5$O$_{15}$(O$_3$PR)$_2$}$_n^{4n-}$ chains linked by {Co$_2$(tpyprz)(H$_2$O$_3$)}$^{4+}$ rods of Figure 10a is
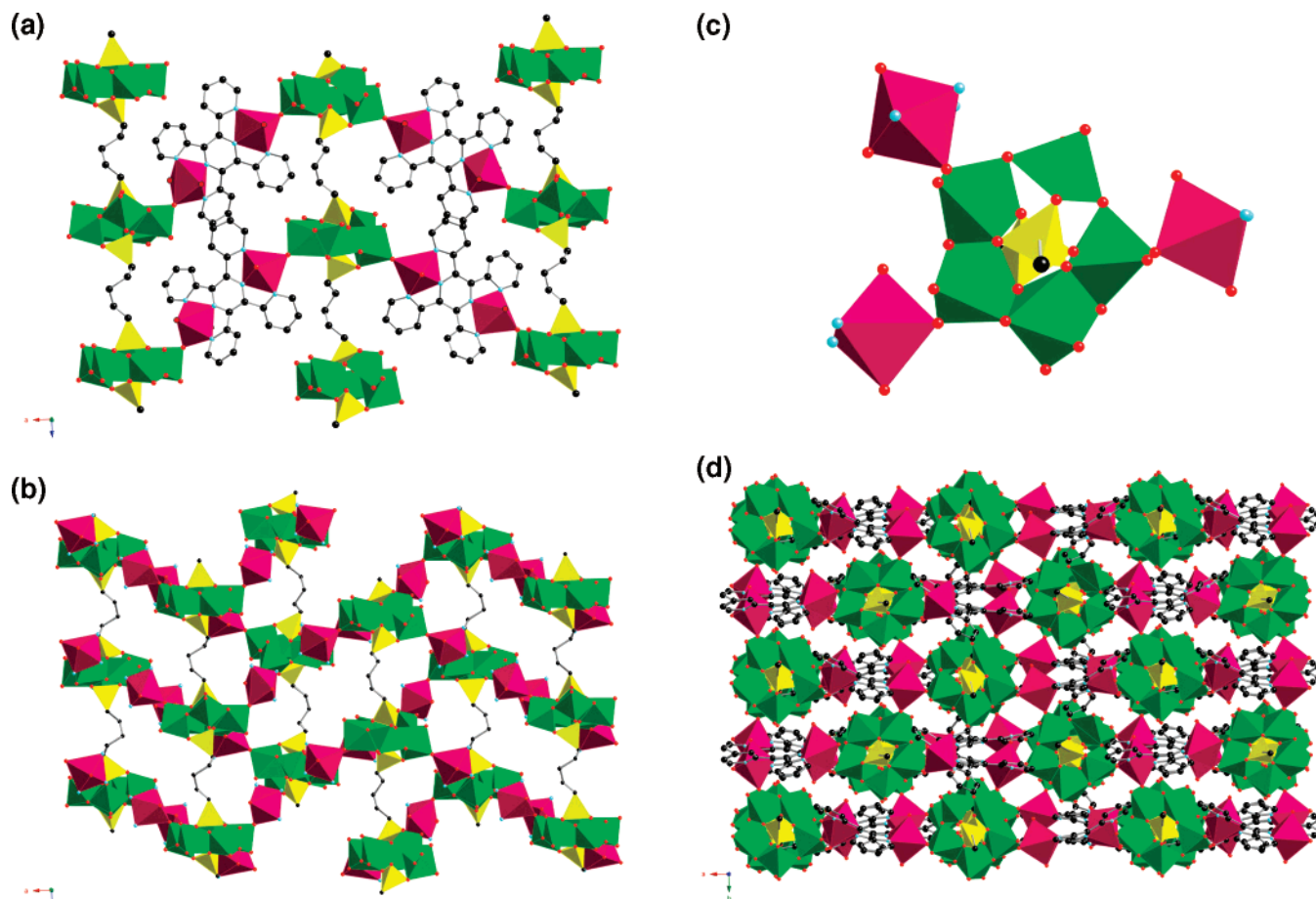
Figure 10. (a) View of one layer of the three-dimensional structure of [{Co$_2$(tpyprz)(H$_2$O)$_3$}Mo$_5$O$_{15}${O$_3$P(CH$_2$)$_5$PO$_3$}]·2.5H$_2$O (**9**·2.5H$_2$O) in the *ac* plane; (b) polyhedral representation of an adjacent layer of **9** upon moving along the *c*-axis; (c) linking of each phosphomolybdate ring to Co(II) sites; (d) view of the structure of **9** along the phosphomolybdate chain axis (parallel to the crystallographic *a*-axis).

observed. This subunit may alternatively be described as {Co$_2$(tpyprz)(H$_2$O)$_3$Mo$_5$O$_{15}$(O$_3$PCH$_2$)$_2$}$_n$ ruffled chains running parallel to the *a*-axis and linked through the pentyl chains of the diphosphonate ligand. However, as the structure evolves along the *c*-direction, the subsequent layer is shifted relative to the first, so as to place the clusters of the chains of the second layer above the rods of the first layer. This shift in the registry of layers along the *c*-direction produces the profile of Figure 10b. Furthermore, each of the cationic rods engages a molybdenum site of a layer above or below the plane in which each Co terminus bonds to a Mo cluster of adjacent chains (Figure 10a). Consequently, each phosphomolybdate cluster is linked to three cationic rods, as shown in Figure 10c.

When the structure of **9**·2.5H$_2$O is viewed along the anionic chain or the *a*-axis, the three-dimensional nature of the structure is apparent (Figure 10d). Furthermore, the virtual layers of alternating phosphomolybdate rings and cationic rods are evident, running parallel to the *a*-axis. These layers are linked through vertex-sharing interactions between Co octahedra and Mo sites of adjacent layers. As a result of this connectivity pattern, a phosphomolybdate chain is linked to two chains in the same layer and two in each adjacent layer.

In comparing the structures of compound **5**, **6** and **9**, the range of connectivity patterns which may be adopted by

materials constructed of analogous building blocks is manifested. Compounds **5** and **6** are constructed from [{Co$_2$-(tpyprz)(H$_2$O)$_3$}Mo$_5$O$_{15}$(O$_3$PR)$_2$] bimetallic layers linked exclusively through the alkane chains of the diphosphonate ligand. The structures diverge as a consequence of differences in the junctions between cationic rods and anionic rings in the plane. In contrast, for compound **9**, the "layers" are linked not only through the diphosphonate tethers but through Co−O−Mo bonding to produce a more densely packed profile when the structures are viewed parallel to the chain axes.

Quite unexpectedly, the structure of the second pentyl derivative [{Co$_2$(tpyprz)(H$_2$O)$_2$}Mo$_6$O$_{18}${O$_3$P(CH$_2$)$_5$PO$_3$}]·2H$_2$O (**10**·2H$_2$O) does not contain the anticipated {Mo$_5$O$_{15}$-(O$_3$PR)$_2$}$^{4-}$ building block but rather the expanded cluster {Mo$_6$O$_{18}$(O$_3$PR)$_2$}$^{4-}$. As shown in Figure 11a, the three-dimensional structure of **10** may be described as bimetallic [{Co$_2$(tpyprz)(H$_2$O)$_2$}Mo$_6$O$_{18}${O$_3$P(CH$_2$)$_5$PO$_3$}]$_n$ layers in the *ac* plane linked through Co−O−Mo bonds along the crystallographic *b*-direction to adjacent layers. The profile of the structure when viewed parallel to the *a*-axis, shown in Figure 11b, is similar to that observed for compound **11**, with the exception that each {Co$_2$(tpyprz)(H$_2$O)$_2$}$^{4+}$ rod engages in an additional interaction between layers to provide three-dimensional rather than two-dimensional connectivity as observed for **11**.
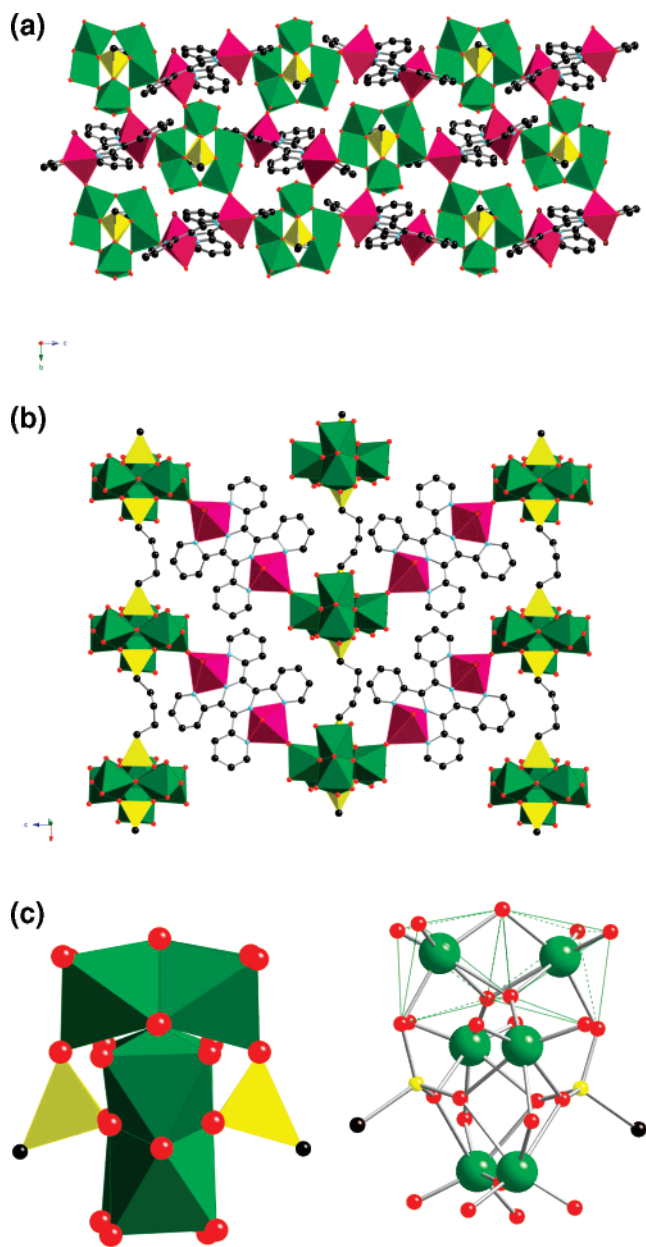
(a)

(b)

(c)

Figure 11. (a) Polyhedral representation of the structure of [{Co$_2$(tpyprz)-(H$_2$O)$_2$}Mo$_6$O$_{18}${O$_3$P(CH$_2$)$_5$PO$_3$}]·2H$_2$O (**10**·2H$_2$O) in the *bc* plane; (b) view of the structure of **10** in the *ac* plane; (c) ball and stick and polyhedral views of the {Mo$_6$O$_{18}$} cluster of **10**.

Each phosphomolybdate cluster exhibits four sites of attachment to the cationic rods at four different Mo centers. Two of the cationic components link the cluster unit to clusters of adjacent chains in a virtual layer and to four clusters in immediately adjacent layers. The other two cationic rods each link the cluster to two clusters of an adjacent layer and to a third in a layer one removed. Thus, each rod links four clusters of three neighboring layers, and each cluster is tethered to eight clusters from four neighboring layers.

The most unusual feature of the structure of **10** is the presence of a novel cluster building block, the hexamolybdate {Mo$_6$O$_{18}$(O$_3$PR)$_2$}$^{4-}$, shown in Figure 11c. The cluster consists of three binuclear subunits of face-sharing Mo octahedra interlinked through corner-sharing interactions.
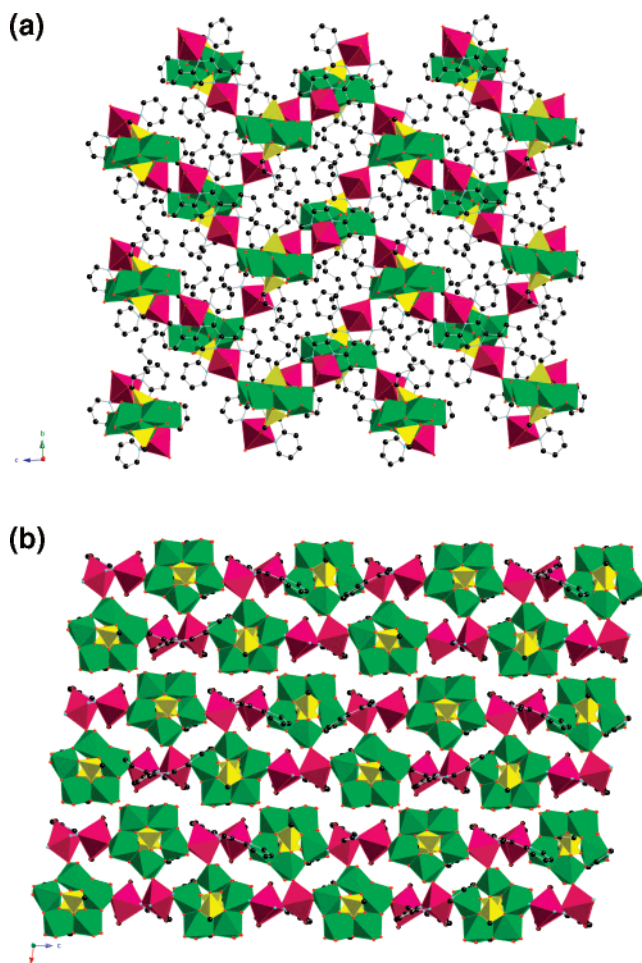
(a)

(b)

Figure 12. (a) Polyhedral view of the structure of [{Co$_2$(tpyprz)(H$_2$O)$_3$}-Mo$_5$O$_{15}${O$_3$P(CH$_2$)$_9$PO$_3$}]·2.5H$_2$O (**11**·2.5H$_2$O) in the *bc* plane; (b) two-dimensional structure of **11** viewed in the *ac* plane.

Four molybdenum sites of two binuclear units are coplanar, while the vector between the molybdenum sites of the remaining diad is normal to the plane. Each phosphonate group links to five molybdenum sites to complete the cluster. While the {Mo$_5$O$_{15}$(O$_3$PR)$_2$}$^{4-}$ building block is extensively precedented in the molecular chemistry of the molybdenum oxides, there is no corresponding molecular analogue for the {Mo$_6$O$_{18}$(O$_3$PR)$_2$}$^{4-}$ building block encountered in the structure of **10**.

(f) [{Co$_2$(tpyprz)(H$_2$O)$_3$}Mo$_5$O$_{15}${O$_3$P(CH$_2$)$_9$PO$_3$}]·2.5H$_2$O. The two-dimensional structure of the nonyldiphosphonate compound [{Co$_2$(tpyprz)(H$_2$O)$_3$}Mo$_5$O$_{15}${O$_3$P(CH$_2$)$_9$PO$_3$}]· 2.5H$_2$O (**11**·2.5H$_2$O) is shown in Figure 12a. The structure consists of the common [Mo$_5$O$_{18}$(O$_3$PR)$_2$]$_n^{4n-}$ anionic chains linked by {Co$_2$(tpyprz)(H$_2$O)$_3$}$^{4+}$ rods into a 2-D slab, which may be described as a double layer comprised of two planar sheets of alternating chains and rods (Figure 12b). Within a sheet, each anionic chain is tethered to two adjacent chains through cationic rods, linking at full extension through the cobalt sites at either terminus. Adjacent pairs of sheets are then connected through additional Co−O−Mo bonds which engage cobalt sites from either sheet in an alternating pattern. Consequently, each phosphomolybdate cluster is linked to three cationic rods, which in turn tether the chain to two adjacent chains in the sheet and to two chains in the
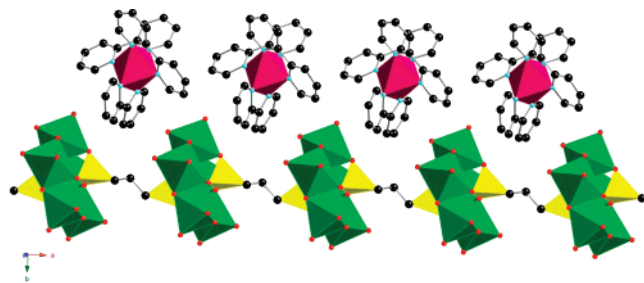
Figure 13. Structure of [Co(bpy)$_3$][Mo$_5$O$_{14}$(OH){HO$_3$P(CH$_2$)$_3$PO$_3$}] (**12**).

Figure 14. View of the structure of [{Co$_2$(phen)$_3$(H$_2$O)}Mo$_5$O$_{15}${O$_3$P(CH$_2$)$_3$-PO$_3$}] (**13**).

neighboring sheet. The loci of connectivity in the phosphomolybdate clusters are three adjacent Mo sites of the ring, including the two sites which engage in the corner-sharing interactions between {MoO$_6$} octahedra.

The connectivity pattern produces a staggered profile of chains and rods in the two sheets of the covalently linked slabs. Adjacent slabs are aligned such that the phosphomolybdate clusters of one slab nestle in the shallow hallows between two clusters of the adjacent slab. Consequently, the slabs are relatively densely perched and the volume accessible to water molecules of crystallization is not extensive, as indicated by the incorporation of ca. 2.5H$_2$O per formula unit.

Although the one-dimensional chain constructed of pentamolybdate clusters linked through diphosphonate tethers is a recurrent theme of the structure of this study, the linkage modes of the cationic components to the anionic chains exhibit considerable diversity. For the family of this study, two, three, or four attachment points at the oxygens of the clusters to the Co(II) sites are observed. To evaluate the potential range of loci of attachment at the clusters, modifications of the cationic component were introduced.

(g) Phases with {Co(2,2′-bpy)$_3$}$^{2+}$, {Co(terpy)$_2$}$^{2+}$, and {Co(phen)$_x$}$^{2+}$ Components. If the coordination sites at the Co(II) were to be saturated by the organonitrogen donors, as in the tris-chelate {Co(bpy)$_3$}$^{2+}$, then the "naked" phosphomolybdate chain should be observed, that is, a structure where the number of points of attachment is zero. This has been accomplished by introducing a large excess of 2,2′-bipyridine in the preparation of [Co(bpy)$_3$][Mo$_5$O$_{14}$-(OH){HO$_3$P(CH$_2$)$_3$PO$_3$}]·H$_2$O (**12**·H$_2$O), whose structure is shown in Figure 13. The structure consists of {Co(bpy)}$^{2+}$ cations, and it represents the first instance of undecorated [Mo$_5$O$_{14}$(OH){HO$_3$P(CH$_2$)$_3$PO$_3$}]$_n^{2n-}$ chains. Charge balance considerations dictate that two oxygen sites of a phosphomolybdate cluster must be protonated. These are readily identified as one doubly bridging Mo–O–Mo oxo site and one P–O–(Mo)$_2$ phosphonate site. Thus, for the protonated Mo–O(H)–Mo site, the average Mo–O bond distance is 2.062(2) Å, while the average Mo–O distance for all other doubly bridging oxo-groups is 1.916(2) Å. Similarly, the P–O(H) distance is 1.570(3)Å, compared to an average of 1.531(3) Å for all other P–O distances.

The same chain structure with {Co(terpy)$_2$}$^{2+}$ cations is observed when excess terpyridine is used in the synthesis for [Co(terpy)$_2$][Mo$_5$O$_{14}$(OH){HO$_3$P(CH$_2$)$_3$PO$_3$}]·H$_2$O (**13**·H$_2$O). In this case, the Mo–O(H)–Mo bond distance is
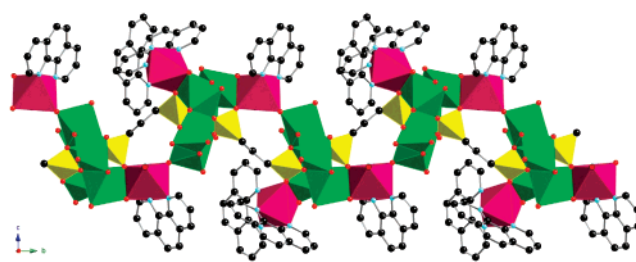
2.053(2) Å, compared to an average distance of 1.912(2) Å for all other doubly bridging Mo–O distances. The P–O(H) distance is 1.560(2) Å, compared to an average P–O distance of 1.529(2) Å.

Similarly, the use of excess Co(II) relative to the organonitrogen donor provided [{Co$_2$(phen)$_3$(H$_2$O)}Mo$_5$O$_{15}$-(O$_3$P(CH$_2$)$_3$PO$_3$)] (**14**), whose structure is shown in Figure 14. In this case, the one-dimensional [Mo$_5$O$_{15}${O$_3$P(CH$_2$)$_3$-PO$_3$}]$_n^{4n-}$ chain is decorated by two distinct Co(II) moieties. The first is a {Co(phen)$_2$}$^{2+}$ unit which edge-shares with a molybdenum site through a multiply bonded oxo-group {Mo=O) and a phosphonate oxygen {P–O–Mo}. The second Co(II) site {Co(phen)(H$_2$O)}$^{2+}$ shares an edge with an Mo site of one cluster through a terminal oxo-group and a {P–O–Mo} phosphonate oxygen donor and bridges to a molybdenum site of an adjacent cluster through a terminal oxo-group. The most noteworthy feature of this structure is the use of five points of attachment to Co(II) sites at each cluster.

(h) Structural Trends and Comparisons. The structures of the study and those of the previously reported M(II)–organonitrogen ligand/Mo$_5$O$_{15}$–diphosphonate subfamilies (M = Ni, Cu) exhibit a variety of linkage modes between the molybdate clusters and the cationic components, ranging in number from zero to five and employing a variety of cluster oxygen sites. As indicated by Figure 15, oxygen atoms at sites 1–5, 7, 8, 10, 13, 14, 16, and 21 participate in bonding in at least one structure. While the majority of structures of this general class exhibit M(II) interactions with terminal {Mo=O} oxo-groups exclusively, five also exhibit {M–O(P)–Mo} linkage to phosphonate oxygen donors. There is a single example [{Cu(terpy)}$_2$Mo$_5$O$_{15}${O$_3$P(CH$_2$)$_4$-PO$_3$}] of participation by bridging oxo-groups {Mo–O–Mo} in bonding to the secondary metal.

The structural chemistry of the Co(II)–organonitrogen/oxomolybdate–organodiphosphonate family of materials reveals the persistence of certain common motifs, which have been previously encountered in the related M(II)–organonitrogen/oxomolybdenum–organodiphosphonates for M(II) = Ni and Cu. A review of the structural chemistry of these materials confirms the persistence of two oxomolybdophosphonate building blocks. When methylenediphosphonate is present as a building block, the tether length precludes extension of the oxomolybdophosphonate substructure through the phosphate groups of the ligand, and consequently the common {Mo$_5$O$_{15}$(O$_3$PR)$_2$}$^{4-}$ building block is not observed. However, the methylenediphosphonate chemistry of the Co-
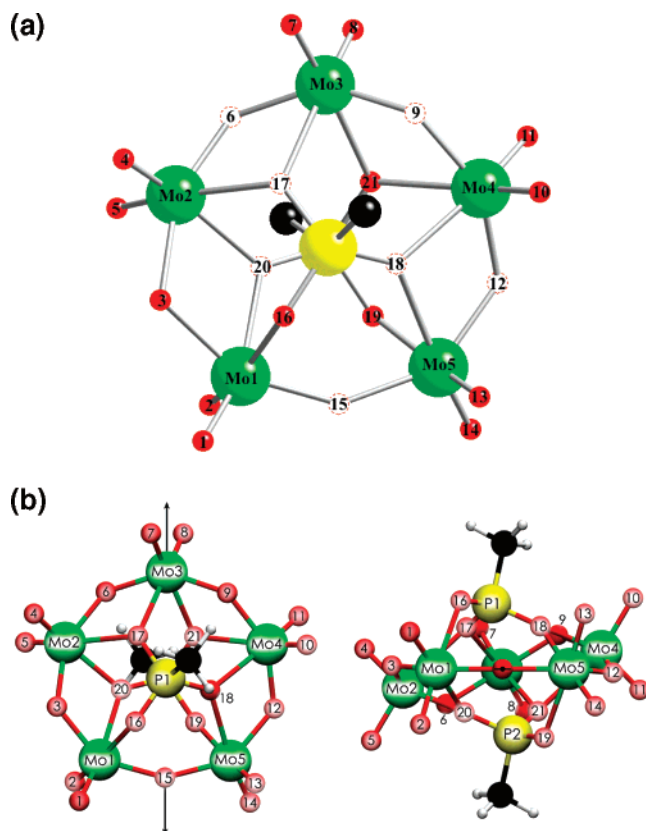
Figure 15. (a) Schematic representation of the $\{Mo_5O_{15}(O_3PR)_2\}^{4-}$ core of the structures of this study. The red-filled oxygen spheres indicate observed attachment sites in the family of materials M(II)−organonitrogen ligand/Mo_5O_{15}−diphosphonate (M = Co, Ni, Cu). The dashed outlines identify oxygen sites which are not used in bonding to the secondary metal organic moieties. (b) Top (left) and front (right) cluster views and atom labeling scheme (green = Mo, red = O, yellow = P, black = C, white = H) for the modeling studies.

(II), Ni(II), and Cu(II) families of materials uniformly exhibits the trinuclear $\{Mo_3O_8(O_3PCH_2PO_3)\}^{2-}$ cluster as a secondary building unit in the form of a single unit, a dimer of clusters, or a chain of clusters.

While the alternative oxomolybdodiphosphonate building block $\{Mo_5O_{15}(O_3PR)_2\}^{4-}$ is nearly ubiquitous in the structural chemistry of the Co(II), Ni(II), and Cu(II) families, the details of the connectivities between building blocks are often quite distinct, as summarized in Table 2. This observation is most readily apparent in the overall dimensionality of the material. As illustrated in Figure 16, for the structures of the general type M(II)−organonitrogen/oxomolybdate−organophosphonate, one-, two- and three-dimensional structures have been identified, although the naive expectation for the linking of anionic oxomolybdodiphosphonate chains and cationic rods of the $\{M_2(tpyprz)\}^{4+}$ subgroup is the formation of two-dimensional materials. In fact, three-dimensional phases are more common than two-dimensional for this limited series of materials. However, the relatively small number of structures renders any conclusions on the dimensional preferences tentative at best. The identities of the organic ligands and the secondary metal are also likely to prejudice the results.

This variability is related to a number of structural determinants, including the identity of the secondary metal
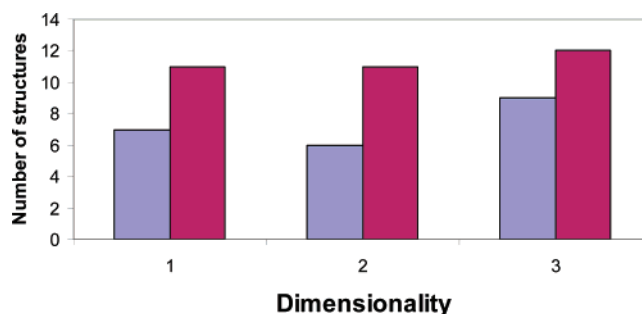

Figure 16. Graphical representation of the distribution of structures of the general type M(II)−organonitrogen/oxomolybdate−organophosphonate among one-, two-, and three-dimensionalities. Blue bar, structures with oxomolybdodiphosphonate chains and $\{M_2(tpyprz)\}^{4+}$ cationic rods as building blocks; red bar, all structures of the Mo_xO_y/diphosphonate/M(II)−organonitrogen families of bimetallic oxides.

component, the tether length of the diphosphonate ligand, the number of attachment points on the molybdate cluster employed in bonding to the secondary metal−ligand subunit, and the coordination mode adopted by the secondary metal component. The influences of the coordination requirements of the secondary metal are most apparent in the contrasting characteristics of Cu(II) with respect to Co(II) and Ni(II).

While Co(II) and Ni(II) display a preference for more or less regular octahedral coordination, Cu(II) displays Jahn−Teller distorted geometries (square planar, 4 + 1 square pyramidal, and 4 + 2 distorted six coordinate). The structural consequences are most apparent when tpyprz is the ligand to the secondary metal. A Cu(II) cation will bind to a terminus of a single tpyprz ligand, thus favoring the $\{Cu_2-(tpyprz)\}^{4+}$ cationic rod with $\{CuN_3O\}$, $\{CuN_3O_2\}$, or $\{CuN_3O_3\}$ coordination geometries adopted upon linking to the oxide chain through one, two, or three attachment points, respectively. In contrast, Co(II) and Ni(II) can adopt regular octahedral geometry by bonding to two tpyprz ligands to produce $\{MN_6\}$ coordination. The extreme examples of this tendency occur in $[Ni_2(tpyprz)_2][Mo_6O_{18}(H_2O)(O_3PC_6H_3)_2]$ and $[Ni_2(tpyprz)_2][Mo_7O_{21}(O_3PCH_2PO_3)]$, where the cationic substructure is present as an isolated $\{Ni(tpyprz)\}_n^{2n+}$ chain. More commonly, there is a balance between the idealized octahedral geometry and the oxophilicity of the M(II) centers which can result in oligomerization which provides $\{M_2-(tpyprz)(H_2O)_x\}^{4+}$, $\{M_2(tpyprz)_2\}^{4+}$, $\{M_3(tpyprz)_2\}^{6+}$, and $\{M_4(tpyprz)_3\}^{8+}$ cationic rods. One consequence of this potential oligomerization is the expansion of structural chemistry of the Co(II) and Ni(II) families in comparison to the Cu(II) materials. This catenation phenomenon is observed in the structures of compounds **2**, **4**, and **7** of this study.

As might be expected there are few examples of structural isomorphism between members of the Cu(II) family and those of the Co(II) and Ni(II) types. Thus, while the compounds $[\{M_2(tpyprz)(H_2O)_2\}(Mo_3O_8)_2(O_3PCH_2PO_3)_2]$, M = Ni, and Cu, are isomorphous, no other isostructural pairs of the Cu/Ni or Cu/Co series are encountered. On the other hand, there are several parallels in the structures of the Co-(II) and Ni(II) series. Thus, compounds **2** and **5** are isostructural with their Ni(II) analogues, while **3** is the structural analogue of the Ni(II) counterpart with $n = 4$ for the diphosphonate tether length.

The structural consequences of the identity of the secondary metal cation are illustrated by comparing the structures of [{Cu₂(tpyprz)(H₂O)₂}Mo₅O₁₅{O₃P(CH₂)₃PO₃}]·2.25H₂O, [{Ni₂(tpyprz)(H₂O)₃}Mo₅O₁₅{O₃P(CH₂)₃PO₃}]·H₂O, and [{Co₂-(tpyprz)(H₂O)₃}Mo₅O₁₅ {O₃P(CH₂)₃PO₃}]·7H₂O (5·7H₂O). While all are three-dimensional and constructed from the same secondary building blocks, [Mo₅O₁₅{O₃P(CH₂)₃PO₃}]ₙ⁴ⁿ⁻ chains and {M₂(tpyprz)(H₂O)ₙ}⁴⁺ rods, the detailed connectivity patterns between the building blocks are quite distinct. It is most noteworthy that the {M₂(tpyprz)(H₂O)ₙ}⁴⁺ secondary building units adopt different linkage modes with respect to the anionic clusters of the chains. This observation reflects in part the variable numbers of aqua ligands *n* which may be incorporated into the rod. Furthermore, the number of available coordination sites at the M(II) centers for linking to the oxygen sites of the phosphomolybdate clusters will be limited by the aqua ligation. There can be considerable variability in the number of aqua ligands per cationic unit of the type {M₂(tpyprz)(H₂O)ₙ}⁴⁺ with *n* taking on values 0−3. Since the aqua ligation cannot be directly controlled in the synthesis, this characteristic of the chemistry renders structural predictability rather problematic.

It is also apparent that the secondary metal subunit does not act simply as a rod connecting two cluster sites on adjacent anionic chains. In fact a survey of the structural chemistry of the M(II)−tpyprz/oxomolybdate−diphosphonate materials reveals that {M₂(tpyprz)(H₂O)ₙ}⁴⁺ subunits may be associated with one, two, three, or four phosphomolybdate clusters. Furthermore, the cationic subunit may bridge clusters of the same chain or clusters on adjacent chains.

The structural chemistry is further complicated by the variability in the numbers and locations of loci of attachment on the phosphomolybdate clusters of the anionic building blocks. Thus, for the common {Mo₅O₁₅(O₃PR)₂}⁴⁻ building block, two to five attachment sites have been observed. Several observations are relevant to this discussion of structural systematics. Only a single example of a "naked" {Mo₅O₁₅(O₃P(CH₂)ₙPO₃)}ₙ⁴ⁿ⁻ chain has been identified. Similarly, there is only one example of five loci of attachment, [{Co₂(phen)₃(H₂O)}Mo₅O₁₅ {O₃P(CH₂)₃PO₃}]. The most common attachment points are terminal oxo-groups {Mo=O}, although nine of twenty-two structures also exhibit cation subunit attachment at {P−O−Mo} oxygen sites of the clusters. There is a single example of attachment at a bridging {Mo−O−Mo} site, [{Cu(terpy)}₂Mo₅O₁₅{O₃P(CH₂)₃-PO₃}].

The patterns of connectivity adopted between the anionic and cationic building block also influence the accessible volume for solvent incorporation. In this regard, it is apparent that the generation of void volume in the layered and framework materials is not related to the tether length of the diphosphonate ligand but rather is related to catenation and the length of the cationic rods. The diphosphonate tether length itself is not an indicator of solvent accessible volume as a consequence of the variability of number and location of attachment points at the phosphomolybdate clusters, as well as the range of relative orientations of anionic and

cationic components which can produce structures with relatively dense frameworks. However, the largest solvent accessible volumes are invariably associated with structures exhibiting catenation in the cationic component, for example [{Co₄(tpyprz)₃}Mo₅O₁₅{O₃P(CH₂)₂PO₃}]·18H₂O and [{Co₃-(tpyprz)(H₂O)₃}(Mo₅O₁₅{O₃P(CH)₃PO₃})₂]·21.4H₂O. Increasing the distance between cluster modal points in the anionic chain is clearly not a sufficient condition for increasing the accessible extraframework volume in these materials.

Modeling Studies. (a) Geometry Optimization of the {Mo₅O₁₅(O₃PCH₃)₂}⁴⁻ Model Cluster. The {Mo₅O₁₅(O₃-PCH₃)₂}⁴⁻ model cluster, extracted as a C_1-symmetry system from the crystal cell, optimizes to a C_2-symmetry minimum energy form at both the B3LYP and BLYP/DND levels of theory, with the rotation axis containing O15 and Mo3 (Figure 15). Supplementary Information Table S1 contains the bond lengths for the experimental and calculated Mo−O and P−O bonds grouped by their C_2-symmetry. The B3LYP and BLYP/DND calculated bond length differences from experiment and the differences between bond lengths of symmetry-related bond pairs in the diffraction studies are provided graphically in Figure 17. The B3LYP (red) and BLYP/DND (blue) calculated bond length differences result from the differences in the two methods, which agree in general trends and are specifically in good agreement in the cases of all μ_3 oxygen distances. The differences in the experimental bond lengths related by C_2-symmetry provide a measure of the degree of [P₂R₂Mo₅O₂₁]⁴⁻ deformation that occurs from crystal interactions (both Co-coordination and hydrogen-bonding). The reported values in Figure 17 are not to be confused with the actual degree of cage deformation from an isolated-molecule limit for the true {Mo₅O₁₅-(O₃PR)₂}⁴⁻ cluster because (a) the interaction-free Mo−O and P−O bond lengths are not experimentally known and (b) the B3LYP and BLYP/DND bond lengths are generally longer than observed, making the use of their values as "average" for calculating the degree of {Mo₅O₁₅(O₃PR)₂}⁴⁻ deformation inappropriate.

The magnitude of the symmetry-related experimental bond length differences correlate directly with the positions of Co-coordination/hydrogen-bonding interactions (Figure 18). The large difference for the Mo1−O1/Mo5−O14 C_2-symmetry bond pair results from Co-coordination to O1 and subsequent deformation of the Mo1 position in the crystal cell. The deformation of the Mo3−O7/Mo3−O8 C_2-symmetry bond pair occurs from the asymmetric hydrogen-bonding of O7 to crystal water D. For oxygen atoms on Mo2 and Mo4, the C_2-related experimental bond length differences are negligible because both sites include Co-coordination to C_2-symmetry-related oxygen atoms (O4 and O11). The deformations for the μ_2 and μ_3 Mo−O bond lengths are localized to differences between Mo1 and Mo5, a result of the Co-coordination to O1 and the induced deformation of Mo1 relative to Mo5.

The B3LYP and BLYP/DND bond length differences from experiment reveal a number of trends that reflect the influence of the crystal cell on {Mo₅O₁₅(O₃PCH₃)₂}⁴⁻
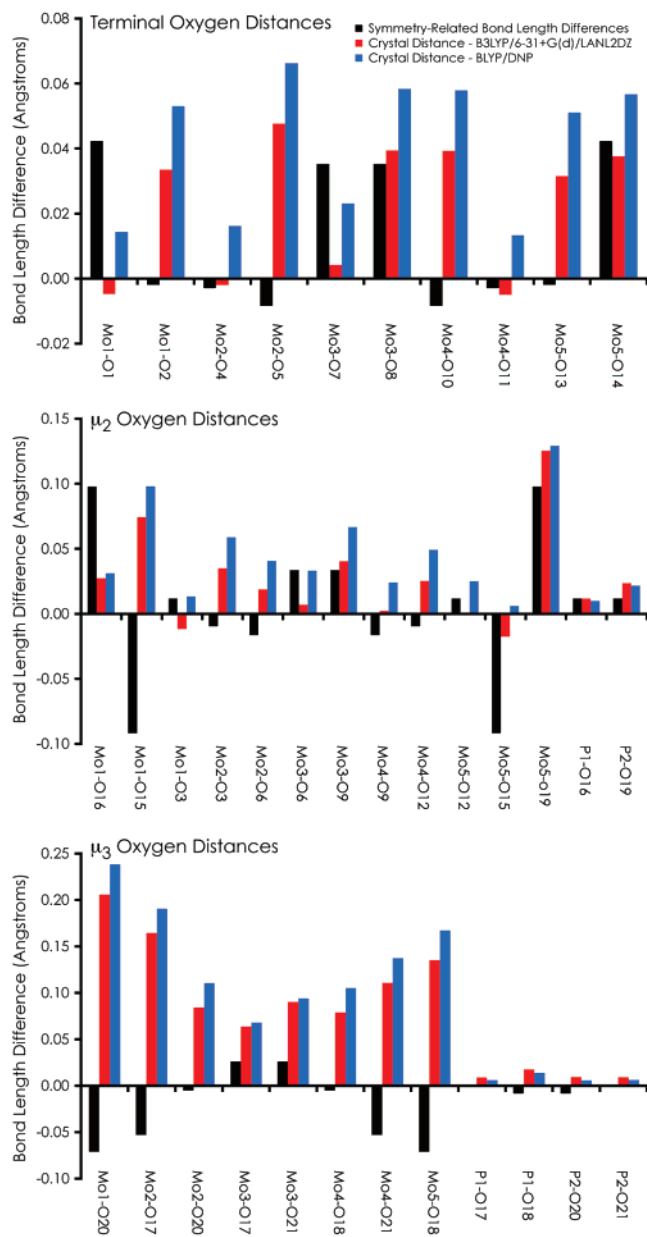
Figure 17. Experimental and calculated bond length differences. Black, bond length differences between Mo−O and P−O bonds related by C_2-symmetry (provided as visual summary and not directly comparable to the other presented data); red, bond length differences between the crystal and B3LYP/6-31+G(d)/LANL2DZ calculations; blue, bond length differences between the crystal and BLYP/DND calculations.

Figure 18. Local environments of the $\{Mo_5O_{15}(O_3PR)_2\}^{4-}$ clusters, showing associated hydrogen-bonding interactions from crystal (A, G) and Co-coordinated (B−F) water molecules (color scheme as per Figure 17, with blue = Co and black = N). Carbon and non-water hydrogen atoms have been omitted for clarify.

deformation. The general trends include (a) an overestimation of Mo−O and P−O bond lengths by both methods and (b) a larger range of disagreement with experiment as the coordination number of the oxygen increases (the range of bond length differences for the terminal oxygen atoms is approximately 0.1 Å; for μ_3 oxygen atoms, this range is approximately 0.35 Å). This broader range for the higher-coordination oxygen atoms reflects the greater sensitivity of their Mo−O bond lengths to environmental factors, where less energy is required for larger deformations. Specific trends in oxygen coordination geometries are summarized below. It is important to note, in all cases, that isolated-molecule calculations are being compared to solid-state results. Trends below are reported as if the disagreement
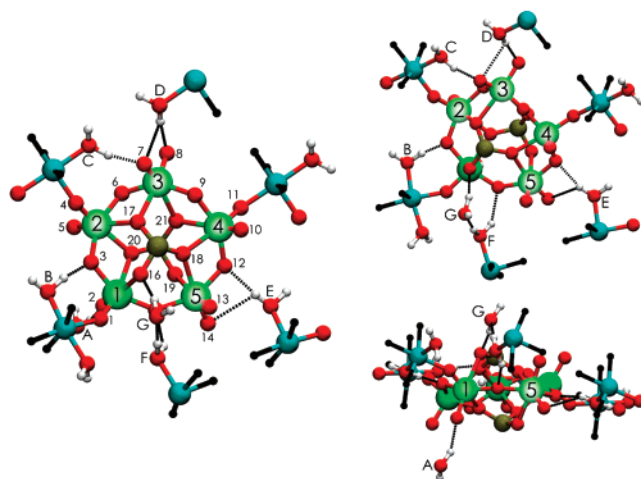
between theory and experiment is exclusively a result of the DFT limitations, but this is performed largely for adding clarity to the presentation of the trends and cannot be argued as entirely a theoretical limitation until a structural charac-terization of the $\{Mo_5O_{15}(O_3PR)_2\}^{4-}$ cluster in the presence of strong crystal interactions becomes available.

The small differences between theory and experiment for bonds Mo1−O1, Mo2−O4, and Mo4−O11 are due to elongation of these Mo−O bonds with O−Co coordination. Bond Mo3−O7 is elongated due to hydrogen-bonding, leading to only a moderate disagreement between theory and experiment. For Mo1−O2, Mo2−O5, Mo3−O8, Mo4−O10, Mo5−O13, and Mo5−O14 (all bonds without Co-coordina-tion or strong hydrogen-bonding to crystal waters) the overestimation of Mo−O bond lengths in the calculations is readily apparent in Figure 17.

The largest differences in the bond length ranges among the μ_2 Mo−O bonds occur in the asymmetric region about Mo1 and Mo5. In the case of O15, Co−O1 coordination at Mo1 and the induced cluster deformation leads to the large asymmetry in the Mo1−O15 and Mo5−O15 bond lengths. Mo1−O16 and Mo5−O19 bond length differences occur as a result of both Co−O coordination to Mo1 and the presence of a hydrogen-bonding interaction to O16. The results of these local environment differences are increases in the Mo1−O16 and Mo5−O15 bond lengths, which yield better agreement with theory and experiment due to their DFT overestimation.

The calculations overestimate μ_3 bond lengths in all cases. While this result is partly a systematic computational result, the sensitivity of these bond lengths to crystal environment and, specifically, the reduction of the volume of $\{Mo_5O_{15}(O_3-PCH_3)_2\}^{4-}$ due to crystal packing interactions cannot be ruled out as an important contributor to the differences between theory and experiment in this case (as well as above). This same trend has been observed in the many isolated-molecule $[Mo_8O_{26}]^{4-}$ calculations, where the absence of crystal packing
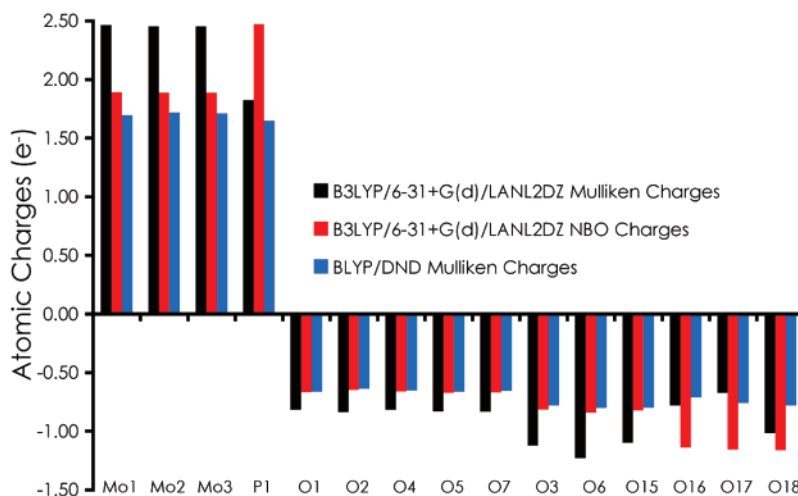
Figure 19. Isolated-molecule population analyses for the symmetry-unique (P, O, Mo) atoms in $[P_2(CH_3)_2Mo_5O_{21}]^{4-}$. See Figure 17 for atom labeling scheme.

and the many associated counterions lead to cage expansion.[71−73] The calculated P−O bond lengths for the μ_3 oxygen atoms are in very good agreement with experiment, indicative of the more direct, formal covalent P−O bonding relative to the Mo−O coordination bonds.

(b) Mulliken and Natural Bonding Orbital (NBO) Population Analyses. The initial purpose of the calculations was to explain the strong preference for terminal Co−O coordination in the solid-state despite an expected preference for coordination to more electron-rich μ_2 oxygen atoms. While the logical reason for this terminal oxygen preference is founded purely in the steric interactions between the bulky substituents defining the remainder of the Co-coordination sphere and the $\{Mo_5O_{15}(O_3PCH_3)_2\}^{4-}$ cage itself, the observation of a few Co−O interactions to O16/O19, O15, and O3/O12 in some of the crystal cells warranted further consideration of the differences of the two oxygen types. Population analyses of the isolated cluster, which have proven useful in a small number of theoretical studies exploring either the general structures[71−73] or the preferred binding positions in other large oxide clusters,[74−76] were therefore undertaken.

The results of Mulliken (B3LYP and BLYP/DND) and NBO (B3LYP) population analyses for the symmetry-unique atoms in $\{Mo_5O_{15}(O_3PCH_3)_2\}^{4-}$ are listed in Supplementary Information Table S2 and plotted in Figure 19 for convenience. A number of general trends appear from these analyses. While Mulliken population analyses are well-known for their basis set sensitivity,[77] the B3LYP and BLYP/DND results agree in the relative magnitudes of the populations for the cluster atoms. The overall wider range

of the B3LYP Mulliken charges may be due to the choice of functional or, more likely, the use of effective core potentials in the B3LYP calculations (all-electron DND basis sets exists for all the atoms in the cluster). The B3LYP NBO population analysis predicts considerable polarization of the P−O bonds in favor of more electron density at the oxygen atoms, resulting in the P atoms being most positive overall and the bound oxygen atoms (the μ_2 O16 and the μ_3 O17 and O18) being most negative.

(c) Preliminary Solid-State BLYP/DN Calculations. The unit cell of $\{Mo_5O_{15}(O_3PR)_2\}^{4-}$ is noteworthy for its relatively small size among the inorganic/organic hybrid molybdate systems catalogued to date. Efforts were therefore undertaken to perform solid-state DFT calculations on this system in order to better understand the deformation of the $\{Mo_5O_{15}(O_3PR)_2\}^{4-}$ due to Co-coordination and the crystal waters. While preliminary results were quite promising, the solid-state optimizations ultimately could not accurately describe the immediate high-spin, unpaired electron coordination sphere of the Co atoms (the result of which was most noticeable in the considerable reduction in the Co−O bond length, the subsequently large increase in the Mo−O bond length, and the overall large relative deformation of the interactions to Mo1, Mo2, and Mo4, those containing Co−O coordination bonds). Further work on this problematic case (and related systems) is ongoing.

Despite this limitation in the use of the solid-state DFT calculations, this first series of optimization attempts at a BLYP/DN level of theory did yield one noteworthy result that does have important ramifications for both the description of the observed $\{Mo_5O_{15}(O_3PR)_2\}^{4-}$ geometry and subsequent solid-state DFT studies of this and related systems. The local hydrogen-bonding interactions between O7 and the nearest Co-coordinated water molecule (D) were found to have a significant affect on the geometry at Mo3, with two arrangements of water molecule (D) yielding two very different interaction motifs. The results of two different crystal cell optimizations are shown in Figure 20. The relevant $O_{cage}−O_{water−D}$ distances are provided in Supple-

(71) Bridgeman, A. J. *J. Phys. Chem. A* **2002**, *106*, 12151.
(72) Allis, D. G.; Rarig, R. S.; Burkholder, E.; Zubieta, J. *J. Mol. Struct.* **2004**, *688*, 11.
(73) Allis, D. G.; Burkholder, E.; Zubieta, J. *Polyhedron* **2004**, *23* (7), 1145.
(74) Kempf, J.-Y.; Rohmer, M.-M.; Poblet, J.-M.; Bo, C.; Bénard, M. *J. Am. Chem. Soc.* **1992**, *114*, 1136.
(75) Long, D.-L.; Kögerler, P.; Farrugia, L. J.; Cronin, L. *Dalton Trans.* **2005**, 1372.
(76) Dolbecq, A.; Lisnard, L.; Mialane, P.; Marrot, J.; Bénard, M.; Rohmer, M.-M.; Sécheresse, F. *Inorg. Chem.* **2006**, *45*, 5898.
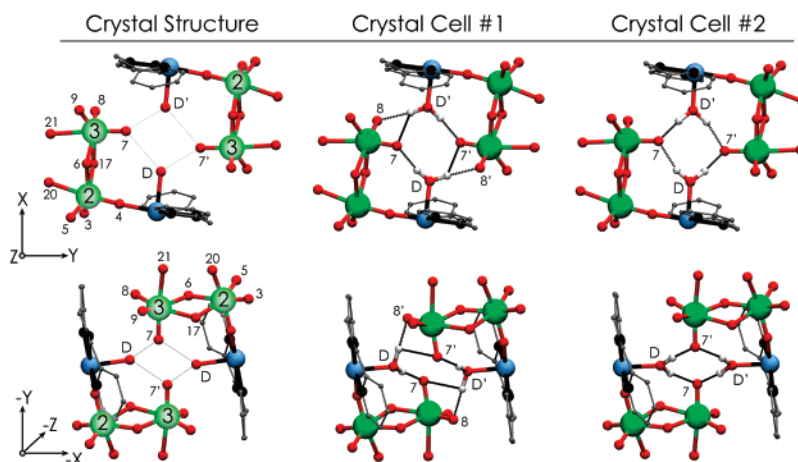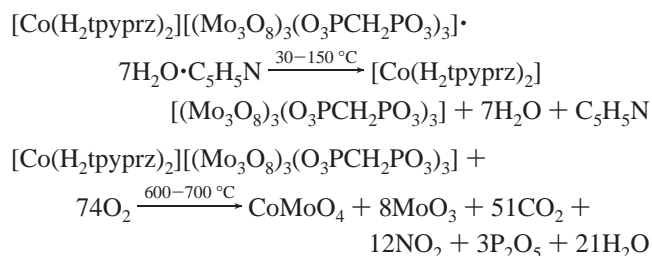(77) Mulliken, R. S.; Politzer, P. *J. Chem. Phys.* **1971**, *55*, 5135.

Figure 20. Mo2 and Mo3 water binding environments in the diffraction experiment (crystal Structure, left), first BLYP/DN geometry optimization with included hydrogen atoms (crystal cell 1, middle), and second BLYP/DN geometry optimization from reoriented hydrogen atoms (crystal cell 2, right). In crystal cell 2, the hydrogen atoms optimize in the plane of the four associated oxygen atoms.

mentary Information Table S3. After the first addition of hydrogen atoms to the crystal cell for the BLYP/DN calculation by forming only a single, direct hydrogen-bond between a crystal water, and one of the O7 atoms (Figure 20), crystal cell no.1 was obtained. In it, the hydrogen-bonding arrangement shown in Figure 20 was that of a highly deformed oxygen hexagon, with each water molecule hydrogen-bonded to three cage oxygen atoms (O7 and O8 on one cage, O7′ on a neighboring cage). This optimized geometry was not consistent with the arrangement of oxygen atoms observed in the crystal cell, which indicated that the four O7−O$_{water}$ distances were within 0.15 Å of each other. The reoptimization of the crystal cell with the water hydrogen atoms oriented directly at both nearby O7 atoms yielded crystal cell no. 2, a final geometry whose better agreement with experiment elucidated the nature of the significant Mo3−O7/Mo3−O8 terminal oxygen bond length differences described above. While the importance of steering quantum calculations is not one that receives much consideration as part of the theoretical analysis of chemical systems, this one instance demonstrates both the benefit of thoroughly considering all of the geometric details of a final calculation and the subtle importance that even a single water molecule may have on the reproduction of a diffraction experiment by solid-state DFT methods. Continued work on this system and similar crystal cells is ongoing.

(d) Mulliken and Natural Bonding Orbital Population Analyses. The Mulliken and NBO population analyses indicate that the higher-coordination oxygen atoms are the positions of highest electron density. From a purely electrostatic perspective, these would then be the most likely binding positions for metal atoms attempting to complete their coordination spheres. The prediction of less negative charge on the terminal oxygen atoms only reinforces the assumption arguable from the diffraction studies alone. Terminal oxygen Co−O coordination in many of the crystal cells characterized in this study is largely a result of the inaccessibility of the empty Co-coordination position due to the steric congestion of the Co ligands. In the crystal cell used for the analysis of $\{Mo_5O_{15}(O_3PR)_2\}^{4-}$ (Figure 20), the

stabilization introduced by Co-coordination to terminal oxygen atoms is also augmented by numerous hydrogen-bonding interactions between both free (A, G) and Co-coordinated (B−F) water molecules. In light of the characterization of the complete crystal site of $\{Mo_5O_{15}(O_3PR)_2\}^{4-}$, it is clear that the weight of an expected preferred binding to a more negative oxygen atom (μ_2) cannot be judged without consideration of the energetic benefits that can come from a combination of weaker Co−O coordination, reduced steric destabilization, and additional stabilizing intermolecular interactions through, specifically for this system, hydrogen-bonding to nearby water molecules.

Thermal Analyses. The thermogravimetric profile of **1** (Supplementary Information Figure S1) illustrates the characteristic pattern for the hydrates of this study of an initial dehydration step at a low-temperature range, followed by pyrolysis of the organic groups at temperatures of 500−700 °C. For compound **1**, a weight loss of ca. 7.1% between room-temperature and 150 °C corresponds to the loss of seven molecules of water of crystallization and the pyridine molecule (7.3% calculated). This is followed by a gradual weight loss of 7% between 250 and 500 °C and a rapid weight loss of ca. 39% between 600 and 700 °C, corresponding to the loss of the organic ligands. The pyrolysis of the diphosphonate to CO_2, H_2O, and P_2O_5 has been observed for a variety of metal diphosphonate materials.[78,79] The overall process is consistent with

$[Co(H_2tpyprz)_2][(Mo_3O_8)_3(O_3PCH_2PO_3)_3] \cdot$
$$7H_2O \cdot C_5H_5N \xrightarrow{30-150\ °C} [Co(H_2tpyprz)_2]$$
$$[(Mo_3O_8)_3(O_3PCH_2PO_3)_3] + 7H_2O + C_5H_5N$$

$[Co(H_2tpyprz)_2][(Mo_3O_8)_3(O_3PCH_2PO_3)_3] +$
$$74O_2 \xrightarrow{600-700\ °C} CoMoO_4 + 8MoO_3 + 51CO_2 +$$
$$12NO_2 + 3P_2O_5 + 21H_2O$$

(78) Cabeza, A.; Ouyang, X.; Sharma, C. V. K.; Avanda, M. A. G.; Bruque, S.; Clearfield, A. *Inorg. Chem.* **2002**, *41*, 2325.
(79) Arnold, D. I.; Ouyang, X.; Clearfield, A. *Chem. Mater.* **2002**, *14*, 2020.
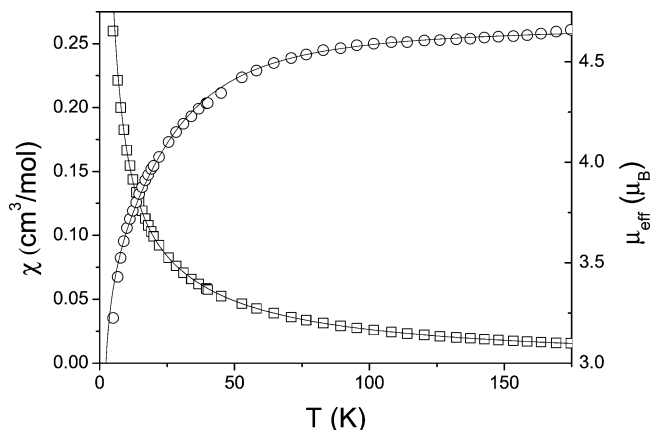
Figure 21. Temperature dependences of the magnetic susceptibility χ ($\square$) and effective magnetic moment μ_{eff} ($\bigcirc$) of [{Co$_4$(tpyprz)$_3$}(Mo$_5$O$_{15}$)$_2$(O$_3$-PCH$_2$CH$_2$PO$_3$)$_2$]·18H$_2$O (**2**·18H$_2$O). The lines drawn through the data are the fits to eqs 1 and 2.

Figure 22. Temperature dependences of the magnetic susceptibility χ ($\square$) and effective magnetic moment μ_{eff} ($\bigcirc$) of [{Co$_2$(tpyprz)(H$_2$O)$_3$}Mo$_5$O$_{15}$-{O$_3$P(CH$_2$)$_3$PO$_3$}]·H$_2$O (**6**·H$_2$O). The lines drawn through the data are the fits to eq 3.

The thermogravimetric profile of **2**·18H$_2$O is similar to that of **1** (Supplementary Information Figure S2), with a 10% weight loss between room temperature and 100 °C attributed to the loss of the water of crystallization (9.1% calculated) and a subsequent loss of ca. 34% assigned to the pyrolysis of the ligands.

The propylene diphosphonate derivatives **4**−**7** exhibit a similar profile, (Supplementary Information Figure S3 for [{Co$_2$(tpyprz)(H$_2$O)$_3$}Mo$_5$O$_{15}${O$_3$P(CH$_2$)$_3$PO$_3$}]·7H$_2$O (**5**·7H$_2$O)). A weight loss of 10.7% between 40 and 165 °C corresponds to the loss of both the water of crystallization and the cobalt bound aqua ligands (11.2% calculated). This is followed by a gradual loss of weight between 325 and 575 °C, whereupon there is a rapid loss of 31.8% by weight. These latter weight losses are consistent with the pyrolysis of the ligands. This profile is consistent throughout the series of materials (Supplementary Information Figures S1−S7): loss of water of crystallization and, in those instances where coordinated water is present, the aqua ligands at temperatures below 150 °C, and a gradual minor weight loss between 200 and ca. 550 °C, followed by a rapid weight loss above 600 °C, corresponding to the combustion of the organic ligands, namely, tpyprz and the diphosphonate.

Magnetism. The temperature-dependent magnetic susceptibilities of several members of the family of materials of this study were investigated. The presence of paramagnetic impurities in all samples of a number of compounds precluded a discussion of the magnetic properties of the entire series. Since the molybdenum sites of all materials of this study are present as Mo(VI) (d^0), the entire contribution to the paramagnetism of the compounds derives from the Co-(II) sites, which are high-spin d^7 ($S = ^3/_2$).

The dependence of magnetic susceptibility χ and effective magnetic moment μ_{eff} on temperature for **2** is shown in Figure 21. The effective moment $\mu_{eff} = \sqrt{8\chi T}$ increases with increasing temperature and reaches a value of 4.67 μ_B at 300 K, which corresponds to one high-spin d^7 Co^{2+} ion. At low temperature, the rapid decrease in magnetic moment suggests a weak antiferromagnetic interaction between Co(II) sites. The experimental results are described using the equation
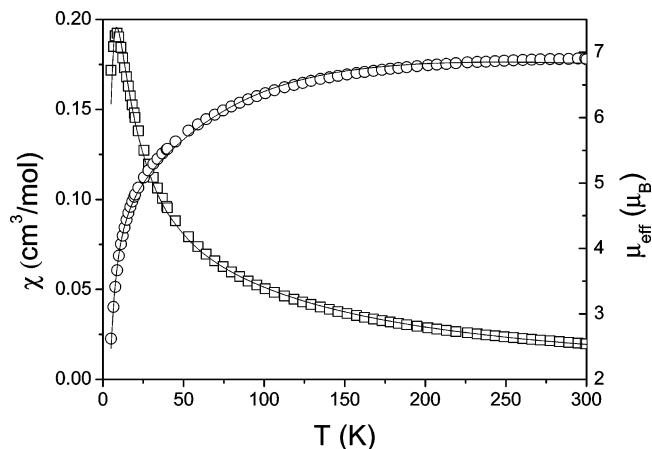
for zero field splitting of spin multiplets ($S = ^3/_2$):

$$\chi = n\frac{N_A g^2 \mu_B^2}{k_B T}\frac{3 + 2/x + (3 - 2/x)e^{-2x}}{4(1 + e^{-2x})} \qquad (1)$$

where n is the number of magnetic ions per molecule, k_B is the Boltzmann constant, N_A is Avrogadro's constant, g is the g-factor, and $x = D/k_B T$, where D is the zero field splitting constant. The calculated susceptibility χ has been corrected for the exchange interaction zJ' between spins:

$$\chi' = \frac{\chi}{1 - (2zJ'/N_A g^2 \mu_B)\chi} \qquad (2)$$

The best fit was obtained for the following parameters: $g = 2.22$, $D/k_B = 45$ K, and $zJ' = -0.35$ K.

Analogous behavior to that of compound **2** is observed for compound **10** (Supplementary Information Figure S8). The effective magnetic moment of **10** increases with increasing temperature to a value of 6.20 μ_B at 300 K. The low-temperature decrease in magnetic moment is consistent with weak antiferromagnetic interactions between Co(II) sites. Using eqs 1 and 2 to fit the experimental results provided the following parameters: $g = 2.30$, $D/k_B = 77$ K, and $zJ'/k_B = -1.3$ K.

The temperature dependences of the magnetic susceptibility and effective magnetic moment of compound **6** are shown in Figure 22. The effective magnetic moment of **6** at 300 K is 6.70 μ_B, which is typical for two spins with $S = ^3/_2$. The low-temperature region shows a magnetic susceptibility maximum, indicative of antiferromagnetic interactions. The susceptibility data for **6** were analyzed using the statistical theory of exchange in paramagnetic cobalt clusters developed by Lines that takes into account the orbital reduction factor k and the spin−orbit coupling parameter λ.[80] The expression for the binuclear Co(II) species is

(80) Lines, M. E. *J. Chem. Phys.* **1971**, *55*, 2977.

$$\chi = \frac{2N_A[g(T)]^2\mu_B{}^2}{k_BT}\frac{1}{3+\exp(-25J/9k_BT)} \quad (3)$$

where J is the intradimer exchange constant and $g(T)$ is a temperature-dependent g-factor, which is determined using the method of ref 63. The best fit was obtained for $k = 0.75$, $\lambda = -175$ K, $J/k_B = -3.6$ K, and $zJ''/k_B = -0.6$ K. The deviation of the theoretical curve from the experimental plot in the low-temperature domain may be related to anisotropic exchange which is not taken into account in the Lines' theory but which is typical for Co(II) clusters. While a good fit of the experimental data for the low-temperature range of such materials can be obtained using the approach of Coronado et al.,[81] in this case the extremely low temperature of the maximum and the presence of a small amount of paramagnetic impurity render the fit ambiguous.

Magnetic susceptibility measurements of complex **5** were performed on polycrystalline samples of compounds at 1000 Oe over the temperature range of 2−300 K. Field-dependent magnetization was performed at 1.8 K over the magnetic field range of 0−70000 Oe. The value of χT at 300 K is 5.46 emu·mol^{-1}·K, which is close to the theoretically expected value for two Co(II) ions ($S = {}^3/_2$, $g = 2.41$) (Figure 23a). The χT value decreases continuously from room temperature and reaches a minimum of 0.16 emu·mol^{-1}·K at 2 K. The temperature dependence of $1/\chi$ between 300 and 6 K approximates the Curie−Weiss behavior with $C = 5.85$ emu·mol^{-1}·K and $\theta = -20$ K. The negative sign of the Curie−Weiss constant indicates spin−orbital coupling as well as antiferromagnetic interactions between Co(II) centers.

Temperature dependence of magnetic susceptibility is more informative. The χ value continuously increases from a room-temperature value of 0.019 emu·mol^{-1}, reaches a maximum of 0.216 emu·mol^{-1} at 7.5 K, and finally decreases again at lower temperatures. Such behavior usually corresponds to antiferromagnetic coupling. It is well-known[82] that, at low temperatures, Co(II) ions behave as effective $S' = {}^1/_2$ centers with effective $g' \approx 4.5$. According to the structural data, **5** may be considered as a dimer with two $S = {}^1/_2$ centers (i.e., Co^{2+} ions), with intradimer Co−Co separations through the tpyprz bridge of 6.84 Å. The variable-temperature magnetic susceptibility data below 30 K were fit to the Bleaney− Bowers equation (eq 4)[83] for two interacting $S = {}^1/_2$ centers:

$$\chi T = \frac{2Ng^2\beta^2/k}{3+\exp(-2J/kT)} \quad (4)$$

using the isotropic exchange Hamiltonian:
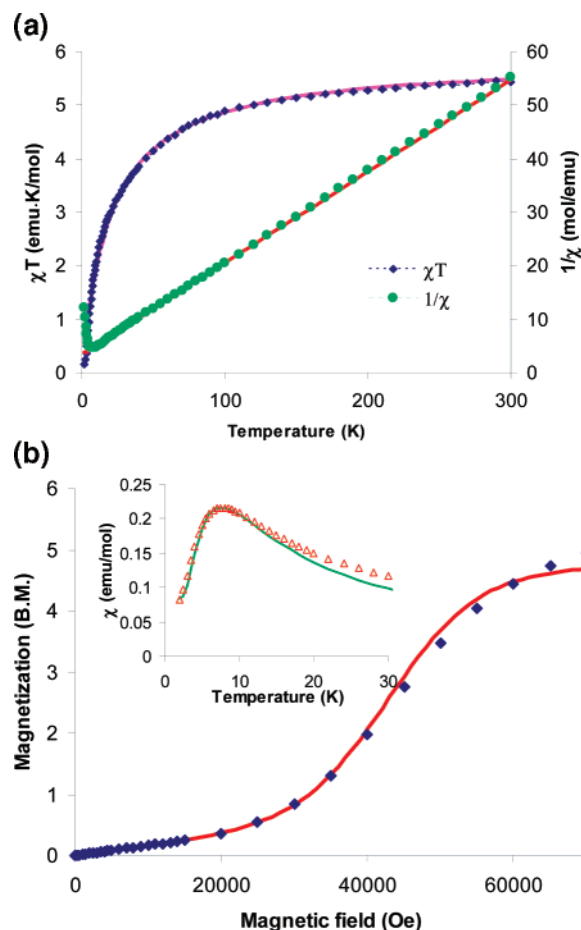
$$\mathcal{H} = 2JS_1S_2 + g\mu_BS_zH \quad (5)$$

(81) Coronado, E.; Drillon, M.; Nugterren, P. R.; de Jongh, L. J.; Beltran, D. *J. Am. Chem. Soc.* **1988**, *110*, 3907.
(82) (a) Carlin, R. L. *Magnetochemistry*; Springer-Verlag: Berlin, 1986. (b) Palii, A. V.; Ostrovsky, S. M.; Klokishner, S. I.; Reu, O. S.; Sun, Z.-M.; Prosvirin, A. V.; Zhao, H.-H.; Mao, J.-G., Dunbar, K. R. *J. Phys. Chem. A* **2006**, *110*, 14003.
(83) (a) Boudreaux, E. A. *Theory and Applications of Molecular Para-magnetism*; Mulay, L. N., Eds.; Wiley: New York, 1976. (b) Kahn, O. *Molecular Magnetism*; VCH: Weiheim, Germany, 1993. (c) Earnshaw, A. *Introduction to Magnetochemistry*; Academic Press: New York, 1968.

Figure 23. (a) Temperature dependence of $\chi T(\diamond)$ and of the inverse susceptibility $1/\chi$ ($\bigcirc$) for [{Co$_2$(tpyprz)(H$_2$O)$_3$}Mo$_5$O$_{15}${O$_3$P{CH$_2$}$_3$PO$_3$}]·7H$_2$O (**5**·7H$_2$O). The solid line corresponds to the best fit to the Curie−Weiss law. (b) Field-dependent magnetization at 1.8 K for **5**. The solid line corresponds to the Magpack simulation to dimer model. The inset shows the temperature dependence of the χ for **5**. The solid line corresponds to the best fit to the Bleaney−Bowers equation (eqs 4 and 5).

where J is the isotropic exchange constant. The best fitting was obtained with $g = 4.21$ and the exchange parameter $J = 4.5$ cm^{-1-}. The model assumed the presence of 4.5% of impurity.

A more precise value of exchange parameter may be obtained from magnetization measurements, which has a sigmoid shape. The diamagnetic ground state dominates below 30 kOe, although at high field the $S = 1$ level would cross, giving a plateau, as shown in Figure 23b. The simulation of the field-dependent magnetization data was carried out using MAGPACK[84] for the Hamiltonian of eq 2. The best simulation was obtained with $g = 4.3$ and the exchange parameter $J = -4.3$ cm^{-1} with 4.5% of impurity.

Conclusions

The compounds of this study have been prepared by conventional hydrothermal methods, which have been demonstrated to afford effective routes to materials constructed of molybdate[85] and metal organic building blocks. In our

(84) Borra's-Almenar, J. J.; Clemente-Juan, J. M.; Coronado, E.; Tsukerblat, B. S. *J. Comput. Chem.* **2001**, *22*, 985.
(85) Michailovski, A.; Patzke, G. R. *Chem. Eur. J.* **2006**, *12*, 9122.

approach to the bottom-up design of oxide materials, a three component system has been adopted, consisting of phosphomolybdate clusters, organic tethering groups, and a secondary metal−organonitrogen ligand subunit which provides charge compensation but may also serve to link to the oxide cluster surface or to connect adjacent clusters of the structure.

The structural chemistry of the Mo_xO_y/diphosphonate/Co-(II)−tpyprz family reveals the persistence of a common motif, the $\{Mo_5O_{15}(O_3PR)_2\}^{4-}$ cluster, which is observed in compounds **2−9**, **11**, and **14**. The absence of the pentamolybdate core in compound **1**, $[Co(H_2tpyprz)_2][(Mo_3O_8)_3(O_3\text{-}PCH_2PO_3)_3]\cdot 7H_2O\cdot C_5H_5N$, reflects the structural determinism of the methylenediphosphonate group which lacks the spatial extension to link pentamolybdate clusters and consequently adopts a chelating geometry to a cluster of smaller size. The structural flexibility of the $\{Mo_5O_{15}(O_3PR)_2\}^{4-}$ cluster and the basicity of the peripheral oxo-groups of the cluster, as well as the tendency of phosphonate groups to occur as protonated species, are manifested in the structures of **12** and **13**. The presence of a hexamolybdate building block in $[\{Co_2(tpyprz)(H_2O)_2\}Mo_6O_{18}\{O_3P(CH_2)_5PO_3\}]\cdot 2H_2O$ (**10·2H₂O**), while unprecedented in solid-state chemistry, is consistent with the observations of larger oligomers in the chemistry of isolated phosphomolybdate clusters.

The profound influences of minor variations in reaction conditions on the structures of organic−inorganic hybrid materials of the molybdenum oxides are also made manifest in the isolation of four distinct phases incorporating propylenediphosphonate as a component, the one-dimensional material **4·5H₂O** and the three-dimensional phases **5·7H₂O**, **6·H₂O**, and **7·21H₂O**.

The structural chemistries of three series of materials of the Mo_xO_y/diphosphonate/M(II)−tpyprz type have now been extensively investigated, namely, those with M(II) = Co-(II), Ni(II), and Cu(II). The identity of the secondary metal M(II) is clearly a significant structural determinant. This is most evident in comparing the structures of the Cu(II) series to those of the Co(II) and Ni(II) families. In the case of the former materials, the Jahn−Teller distorted geometries associated with the Cu(II) site provide a range of coordination geometries in association with the tpyprz ligand and the phosphomolybdate clusters: $\{CuN_3O\}$, $\{CuN_3O_2\}$, and $\{CuN_3O_3\}$. In contrast, for the Co(II) and Ni(II) series, more regular octahedral geometries prevail, and the $\{MN_3O_3\}$ coordination geometry is ubiquitous.

As expected from these arguments, structural isomorphism between the Cu(II) series and the two M(II) series (M = Co, Ni) is rarely encountered. In fact, there is a single case: $[\{M_2(tpyprz)(H_2O)\}(Mo_3O_8(HO_3PCH_2PO_3)_2]$ (M = Ni, Cu). However, since Co(II) and Ni(II) both favor six-coordinate geometries, we might naively expect that materials with the same diphosphonate component would adopt identical structures. In fact, there is a single instance of isomorphism for the Co(II) ad Ni(II) series, $[\{M_4(tpyprz)_3\}(Mo_5O_{15})_2(O_3PCH_2CH_2PO_3)_2]\cdot xH_2O$.

The relevant observation is the variability of the numbers and locations on the phosphomolybdate clusters of the secondary metal−tpyprz rods that link clusters. The variability of attachment modes of M(II)−tpyprz units to peripheral cluster oxygen donors reflects the relatively uniform charge distribution of the cluster surfaces. The attachment of M(II)−tpyprz groups presumably reflects charge density matching,[86] steric and packing considerations.

It is noteworthy that aqua coordination to the $\{MN_3O_6\}$ sites also has profound structural consequences. Thus, the M(II) site for Co and Ni upon coordinating to a single tpyprz ligand may complete its coordination geometry by bonding to a second tpyprz group to give catenation through $\{MN_6\}$ units or to provide $\{M(tpyprz)_2\}^{2+}$ cations, by attaching to three oxygen donors from phosphomolybdate clusters, or by bonding to some combination of phosphomolybdate donors and aqua ligands. Focusing on structures containing the pentamolybdate core, $[\{M_2(tpyprz)(H_2O)_x\}Mo_5O_{15}\{O_3P(CH_2)_n\text{-}PO_3\}]$, three of six Ni(II) structures exhibit aqua coordination and five of nine Co(II) species incorporate aqua ligands. Such variable coordination modes render predictability of structure an elusive goal. While some structural systematics are beginning to emerge, the exquisite synthetic control of organic chemistry has yet to be realized.

Finally, it is noteworthy that while hydrothermal syntheses of aluminosilicates proceed under kinetic control, thermodynamics appear to play a dominant role in the formation of metal organic hybrid scaffolds.[87] For example, there is no apparent change in compositions as a function of reaction times. Similarly, studies of cobalt succinates have shown the importance of thermodynamic control.[88,89] On the other hand, highly porous materials prepared at low temperature, such as $[Zn_4O(O_2CC_6H_4CO_2)_3]$,[90] form under kinetic control, suggesting that this question remains open and in need of further study.

Supporting Information Available: Tables of atomic positional parameters, bond lengths, bond angles, anisotropic temperature factors and calculated hydrogen atom position for **1−14** in CIF format, tables of experimental and calculated (BLYP/DND and B3LYP) interatomic distances (Table S1), isolated-molecule population analyses for the symmetry-unique atoms in $[P_2(CH_3)_2Mo_5O_{21}]^{4-}$ (Table S2), and O7/O8−O$_{water-D}$ interatomic distances (in angstroms) in the experimental and two solid-state BLYP/DN crystal cells (Table S3), thermogravimetric analysis plots for compounds **1**, **2**, and **4−8** (Figures S1−S7), and magnetic susceptibility plot for compound **10** (Figure S8). This material is available free of charge via the Internet at http://pubs.acs.org.

IC701573R

(86) Maggard, P. A.; Bodyle, P. D. *Inorg. Chem.* **2003**, *42*, 4200.
(87) Cheetham, A. K.; Rao, C. N. R.; Feller, R. K. *Chem. Commun. (Cambridge)* **2006**, 4780.
(88) Forster, P. M.; Stock, N.; Cheetham, A. K. *Angew. Chem., Int. Ed.* **2005**, *44*, 7608.
(89) Forster, P. M.; Burbank, C. R.; Livage, C.; Ferey, G.; Cheetham, A. K. *Chem. Commun. (Cambridge)* **2004**, 368.
(90) Eddaoudi, M.; Kim, J.; Rosi, N.; Vodak, D.; Wachter, J.; O'Keefe, M.; Yaghi, O. M. *Science* **2002**, *295*, 469.